J. Fluid Mech. (2024), *vol*. 985, A47, doi:10.1017/jfm.2024.323

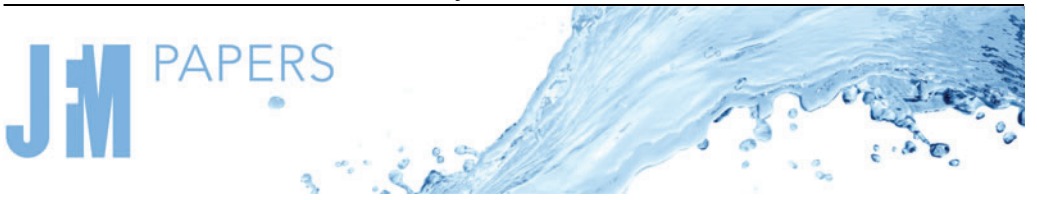

Non-locality of mean scalar transport in two-dimensional Rayleigh–Taylor instability using the macroscopic forcing method

D.L.O.-L. Lavacot[1,2,†], J. Liu[1], H. Williams[1,2], B.E. Morgan[2] and A. Mani[1]

[1]Department of Mechanical Engineering, Stanford University, Stanford, CA 94305, USA

[2]Lawrence Livermore National Laboratory, Livermore, CA 94550, USA

(Received 22 March 2023; revised 9 February 2024; accepted 25 March 2024)

The importance of non-locality of mean scalar transport in two-dimensional Rayleigh–Taylor Instability (RTI) is investigated. The macroscopic forcing method is utilized to measure spatio-temporal moments of the eddy diffusivity kernel representing passive scalar transport in the ensemble averaged fields. Presented in this work are several studies assessing the importance of the higher-order moments of the eddy diffusivity, which contain information about non-locality, in models for RTI. First, it is demonstrated through a comparison of leading-order models that a purely local eddy diffusivity is insufficient to capture the mean field evolution of the mass fraction in RTI. Therefore, higher-order moments of the eddy diffusivity operator are not negligible. Models are then constructed by utilizing the measured higher-order moments. It is demonstrated that an explicit operator based on the Kramers–Moyal expansion of the eddy diffusivity kernel is insufficient. An implicit operator construction that matches the measured moments is shown to offer improvements relative to the local model in a converging fashion.

Key words: turbulent mixing, turbulence modelling

1. Introduction

Rayleigh–Taylor instability (RTI) is a phenomenon that occurs when a heavy fluid is accelerated into a light fluid. Specifically, RTI occurs when the following are present: (1) a density gradient, (2) an acceleration (associated with the body force) in the direction opposite to that of the density gradient, and (3) a perturbation at the interface of the two fluids. RTI is present in many scientific and engineering applications, such as supernovae

† Email address for correspondence: dlol@stanford.edu

© The Author(s), 2024. Published by Cambridge University Press. This is an Open Access article, distributed under the terms of the Creative Commons Attribution licence (http://creativecommons.org/licenses/by/4.0), which permits unrestricted re-use, distribution and reproduction, provided the original article is properly cited.

https://doi.org/10.1017/jfm.2024.323 Published online by Cambridge University Press

(Gull 1975) and inertial confinement fusion (ICF) (Lindl 1995; Zhou 2017). In the case of ICF, RTI occurs when a perturbation forms between the outer heavy ablator and the inner light deuterium gas, which causes premature mixing in the target, thereby greatly reducing the efficiency of the process. Thus RTI is of great interest to scientists and engineers, especially in the context of ICF.

During a typical ICF experiment design process, a Reynolds-averaged Navier–Stokes (RANS) approach is often utilized to model the role of hydrodynamic instabilities such as RTI. This is despite the fact that RTI can be more accurately predicted using high-fidelity methods like direct numerical simulations (DNS) (Youngs 1994; Cook & Dimotakis 2001; Cook & Zhou 2002; Cabot & Cook 2006; Mueschke & Schilling 2009) and large eddy simulations (LES) (Darlington, McAbee & Rodrigue 2002; Cook, Cabot & Miller 2004; Cabot 2006). Motivation for development of RANS models for various engineering applications like ICF can be understood by considering the computational cost of each method. DNS requires resolution of the smallest turbulent scales, and LES the energy-containing scales, which are still much smaller than the macroscopic physics (i.e. averaged fields) of engineering interest. On the other hand, by design, RANS must resolve only macroscopic scales, thereby requiring much lower computational cost. Thus RANS models are commonly used in engineering practice, especially in design optimization, where hundreds of thousands of simulations are often performed. Such is especially the case in designing targets for ICF experiments (Casey *et al.* 2014; Khan *et al.* 2016). Due to the utility of RANS in such applications, the need for predictive RANS models remains salient.

Models of varying complexities have been applied to the RTI problem. Among the types used most commonly are two-equation models. One such model is the ubiquitously used k-ε model (Launder & Spalding 1974). In particular, Gauthier & Bonnet (1990) introduced algebraic relations for some closures to satisfy realizability constraints for the model to be valid under the strong gradients of RTI. Another popular two-equation model is the k-L model; a version was introduced by Dimonte & Tipton (2006) for RTI. One appeal of the k-L model is its inclusion of a transport equation for turbulence length scale L (in place of the transport equation for ε in k-ε) that can be related to the initial interface perturbation. The self-similarity of turbulent RTI is leveraged to set the model coefficients.

These two-equation models rely on the gradient diffusion approximation for the turbulent mass flux closure. The gradient diffusion approximation rests on the assumption that turbulence transports quantities in a manner similar to Fickian diffusion. Importantly, this approximation implies purely local dependence of the mean turbulent flux on the mean gradient, ignoring history effects and gradients at nearby points in space. However, this approximation may not be valid for mean scalar transport. Specifically, the turbulent mass flux contains features that the gradient diffusion approximation cannot capture (Denissen *et al.* 2014; Morgan & Greenough 2015), so a local coefficient may not be enough to scale the mean gradient to model turbulent mass flux.

Non-locality in RTI has been studied in experiments and simulations. Clark, Harlow & Moses (1997) analysed data from turbulent RTI experiments, and compared the pressure–strain correlation and pressure production due to turbulent mass flux, suggesting spatial non-locality of pressure effects. Studies using DNS by Ristorcelli & Clark (2004) and experiments by Mueschke, Andrews & Schilling (2006) have also examined non-locality of RTI in the context of two-point correlations. Thus the non-local nature of RTI is well known, and work has been done to capture this non-locality in models. For example, two-point closures to account for non-locality in RTI have been developed by several authors for RANS (Clark & Spitz 1995; Steinkamp, Clark & Harlow 1999*b*,*a*;

https://doi.org/10.1017/jfm.2024.323 Published online by Cambridge University Press

Pal *et al.* 2018; Kurien & Pal 2022) and LES (Parish & Duraisamy 2017). While these works attempt to address the effects of non-locality in RTI, they do so without directly studying the form of the non-local operator.

Several authors have studied ways to directly measure the non-local eddy diffusivity in other canonical flows. One such approach involves application of the Green's function. The Green's function approach starts from analytical derivations of relations between turbulent fluxes and mean gradients, which was done by Kraichnan (1987). Hamba (1995) then introduced a reformulation of these relations appropriate for numerical computation of non-local eddy diffusivities, which has been applied to study channel flow (Hamba 2004) and, most recently, homogeneous isotropic turbulence (HIT) (Hamba 2022).

A different approach to determining non-local eddy diffusivities is the macroscopic forcing method (MFM) by Mani & Park (2021). In contrast to the Green's function approach, MFM is derived by considering arbitrary forcing added directly to the transport equations, with its formulation rooted in linear algebra. Additionally, MFM offers extensions to the Green's function approach by utilization of forcing functions that are not of the form of a Dirac delta. Harmonic forcing has been utilized to derive analytical fits to non-local operators in Fourier space (Shirian & Mani 2022). Additionally, forcing polynomial mean fields using the inverse MFM offers a computationally economical path for determination of spatio-temporal moments of the eddy diffusivity operator in conjunction with the Kramers–Moyal expansion, as opposed to computation of the moments from a full MFM analysis through post-processing (Mani & Park 2021). Previous works using MFM have revealed turbulence operators for a variety of flows. Shirian & Mani (2022) and Shirian (2022) measured non-local operators in space and time in HIT. Though the spatial non-local operator was measured in HIT, it was applied to a turbulent round jet, and was shown to match experiments more closely than the purely local Prandtl mixing length model. MFM has also been applied to turbulent wall-bounded flows, including channel flow (Park & Mani 2023*b*) and separated boundary layers (Park, Liu & Mani 2022; Park & Mani 2023*a*), to measure the anisotropic but local eddy diffusivity. In those flows, incorporation of the MFM-measured anisotropic eddy diffusivity improved RANS model predictions significantly, and remaining model errors were attributed to missing non-local effects.

It is with a motivation towards RANS model improvement that the present work seeks to understand non-locality of closure operators governing turbulent scalar flux transport in RTI using MFM. Note that it is not intended for MFM to supplant current RANS models. Instead, MFM is an analysis tool that can be used to assess models and discover the necessary characteristics for accurate models. Here, MFM allows for direct measurement of non-local closure operators, which has not yet been done in RTI. This new knowledge of non-locality of the mean scalar transport closure operator in RTI will aid in the development of improved RANS models used for studying ICF.

It is important to note that this work presents MFM measurements for a simplified RTI problem: the flow is two-dimensional, incompressible and low Atwood number, and only passive scalar mixing is considered. Since the eddy diffusivity is not universal, the MFM measurements of its moments presented here cannot be extended directly to more complex RTI. However, valuable insight into trends in the eddy diffusivity for mean scalar transport in RTI can be gained in this work. This follows the common process for developing turbulence models, where models are first designed for simpler flows, then tested on and adjusted for more complex flows. In this work, MFM is performed on a simplified RTI problem to give a preliminary look into the eddy diffusivity of Rayleigh–Taylor-type flows, but future work will involve extensions to more complex flow characteristics that

https://doi.org/10.1017/jfm.2024.323 Published online by Cambridge University Press

are closer to the practical flow observed in ICF capsules. The intent of this work is to present MFM as a tool for determining characteristics of the eddy diffusivity of a flow (i.e. its non-locality and the importance of its higher-order moments) that a model should satisfy in order to accurately predict mean scalar transport. The current work will inform future studies with additional complexities, including three-dimensionality, finite Atwood number, compressibility, and coupling with momentum.

This work is organized as follows. First, an overview of RTI is covered briefly in § 2. Next, § 3 gives an overview of the mathematical methods used in this work, including: (1) the generalized eddy diffusivity and its approximation via a Kramers–Moyal expansion; (2) MFM and its application for finding the eddy diffusivity moments; (3) self-similarity analysis. Simulation details, including the governing equations and the computational approach, are given in § 4. Finally, results of several studies on the importance of higher-order eddy diffusivity moments as well as assessments of suggested operator forms incorporating non-locality of the eddy diffusivity for mean scalar transport in RTI are presented in § 5. The results show that non-locality of the eddy diffusivity is important in mean scalar transport of the RTI problem studied here, and RANS models incorporating this non-locality result in more accurate predictions than in leading-order models.

2. Brief overview of RTI

RTI is characterized by spikes (heavy fluid moving into light fluid) and bubbles (light fluid into heavy fluid). The mixing widths of these spikes and bubbles are denoted as h_s and h_b, respectively, and the mixing half-width is defined as $h = (h_s + h_b)/2$. The behaviours of these quantities in RTI are dependent on the Atwood number, defined as

$$A = \frac{\rho_H - \rho_L}{\rho_H + \rho_L}. \tag{2.1}$$

Here, ρ_H and ρ_L are the densities of the heavy and light fluids, respectively. In the limit of low Atwood number and late time, the mixing layer width is expected to reach a self-similar state of growth that scales quadratically with time:

$$h \approx \alpha A g t^2, \tag{2.2}$$

where α is the mixing width growth rate. The mixing width growth rate can also be viewed as the net mass flux through the midplane (Cook *et al.* 2004). In this case, α can also be written as

$$\alpha = \frac{\dot{h}^2}{4Agh}, \tag{2.3}$$

where $\dot{h}$ is the time derivative of h. In the limit of self-similarity, these two definitions of α are expected to converge to the same value.

In a simulation, h can be measured as

$$h \equiv 4 \int \langle Y_H(1 - Y_H) \rangle \, \mathrm{d}y, \tag{2.4}$$

where Y_H is the mass fraction of the heavy fluid (therefore $Y_L = 1 - Y_H$ is the mass fraction of the light fluid), and $\langle * \rangle$ denotes averaging over realizations and homogeneous direction x. An alternative definition used in works such as Cabot & Cook (2006) and

https://doi.org/10.1017/jfm.2024.323 Published online by Cambridge University Press

Morgan *et al.* (2017) is

$$h_{hom} \equiv 4 \int \langle Y_H \rangle \left(1 - \langle Y_H \rangle\right) \, \mathrm{d}y. \tag{2.5}$$

This definition is particularly useful, since it allows h to be determined solely based on the RANS field. That is, there is no closure problem in determining h with this definition. Thus this is the h reported in this work.

From these two definitions, a mixedness parameter ϕ can be defined, which can be interpreted as the ratio of mixed to entrained fluid (Youngs 1994; Morgan *et al.* 2017):

$$\phi \equiv \frac{h}{h_{hom}} = 1 - 4 \frac{\int \langle Y_H' Y_H' \rangle \, \mathrm{d}y}{h_{hom}}. \tag{2.6}$$

In the limit of self-similarity, ϕ is expected to approach a steady-state value.

A metric for turbulent transition is the Taylor Reynolds number

$$Re_T = \frac{k^{1/2} \lambda}{\nu}, \tag{2.7}$$

where $k = \langle u_i' u_i' \rangle / 2$ is the turbulence kinetic energy, and λ is the effective Taylor microscale, approximated by

$$\lambda = \sqrt{\frac{10 \nu L}{k^{1/2}}}. \tag{2.8}$$

Here, the turbulence length scale L can be approximated as $\frac{1}{5}$ of the mixing layer width (Morgan *et al.* 2017). The large-scale Reynolds number can also be examined (Cabot & Cook 2006):

$$Re_L = \frac{h_{99} \dot{h}_{99}}{\nu}, \tag{2.9}$$

where h_{99} is the mixing width based on 1–99 % mass fraction. Dimotakis (2000) determined that the criterion for turbulent transition is when $Re_T > 100$ or $Re_L > 10\,000$.

3. Mathematical methods

3.1. *Model problem*

In this work, a two-dimensional (2-D), non-reacting flow with two species – a heavy fluid over a light fluid – is considered, with gravity pointing in the negative y-direction. It must be noted that the behaviour of 2-D RTI is significantly different from three-dimensional (3-D) RTI, the latter of which is more relevant to problems of engineering interest. It is well known that while 2-D RTI is unsteady and chaotic, it is not strictly turbulent, since turbulence is a characteristic of 3-D flows. In addition, 2-D RTI has a faster late-time growth rate, develops larger structures, and is ultimately less well mixed. These differences have been studied in RTI by Cabot (2006) and Young *et al.* (2001), and in Richtmyer–Meshkov instability by Olson & Greenough (2014).

For this study, 2-D RTI is chosen as the model problem instead of 3-D RTI, since it is a good simplified setting for understanding non-locality in RTI through the lens of the MFM. Specifically, 2-D RTI simulations are much less computationally expensive than those of 3-D RTI, and MFM requires many simulations to attain statistical convergence. Thus 2-D RTI remains the focus of this work, with the hope that the understanding of non-locality in this flow could be extended to non-locality in 3-D RTI.

https://doi.org/10.1017/jfm.2024.323 Published online by Cambridge University Press

In this 2-D problem, x is the homogeneous direction. In addition, there is no surface tension, the Atwood number and Mach number (Ma) are finite but small, and the Péclet number (Pe) is finite but large.

3.2. *Generalized eddy diffusivity and higher-order moments*

In this work, the effect of non-locality on mean scalar transport is of interest, so analysis begins with the scalar transport equation under the assumption of incompressibility:

$$\frac{\partial Y_H}{\partial t} + \boldsymbol{\nabla} \cdot (\boldsymbol{u} Y_H) = D_H \, \nabla^2 Y_H, \tag{3.1}$$

where $\boldsymbol{u}$ is the velocity vector, and D_H is the molecular diffusivity of the heavy fluid.

After Reynolds decomposition and averaging, this becomes

$$\frac{\partial \langle Y_H \rangle}{\partial t} + \boldsymbol{\nabla} \cdot (\langle \boldsymbol{u} \rangle \langle Y_H \rangle) = -\frac{\partial \langle v' Y_H' \rangle}{\partial y} + D_H \, \nabla^2 \langle Y_H \rangle. \tag{3.2}$$

In this work, large Pe (the ratio of advective transport rate to diffusive transport rate) and small A are assumed. The former assumption means that molecular diffusion is negligible, and the latter yields $\langle u_i \rangle = 0$, allowing the advective term to drop. Equation (3.2) becomes

$$\frac{\partial \langle Y_H \rangle}{\partial t} = -\frac{\partial \langle v' Y_H' \rangle}{\partial y}. \tag{3.3}$$

The term $\langle v' Y_H' \rangle$ is the turbulent scalar flux, and this is the unclosed term that needs to be modelled.

As mentioned previously, one reason why the gradient diffusion approximation used to model this term is inaccurate is that it assumes locality of the eddy diffusivity. This assumption can be removed by instead considering a generalized eddy diffusivity that is non-local in space and time, as demonstrated by Romanof (1985) and Kraichnan (1987). For 2-D RTI, such a model reduces to

$$-\langle v' Y_H' \rangle (y, t) = \iint D(y, y', t, t') \left. \frac{\partial \langle Y_H \rangle}{\partial y} \right|_{y', t'} \mathrm{d}y' \, \mathrm{d}t'. \tag{3.4}$$

Here, y is the spatial coordinate in averaged space, t is the time at which the turbulent scalar flux is measured, y' is all points in averaged space, and t' is all points in time. This definition is exact for passive scalar transport, including in the case studied in this work.

This non-local eddy diffusivity can also be viewed as a two-point correlation. This was first described by Taylor (1922) in homogeneous turbulence. Through Lagrangian statistical analysis, Taylor derived the following relation between diffusivity and velocity correlations:

$$D_{ij} = \int_0^\infty \left\langle v_i(t) \, v_j(t + t') \right\rangle \mathrm{d}t'. \tag{3.5}$$

Work by Shende, Storan & Mani (2023) has shown that the MFM recovers this Lagrangian formulation for eddy diffusivity in homogeneous flows. It should be noted that the above definition is not valid for inhomogeneous RTI (again, the exact definition of eddy diffusivity for the studied flow is the one in (3.4)), but the intent here is to provide another interpretation of the MFM that is more aligned with the well-understood two-point correlations.

https://doi.org/10.1017/jfm.2024.323 Published online by Cambridge University Press

The eddy diffusivity kernel can be approximated by Taylor-series-expanding the scalar gradient locally about y and t, which results in the following Kramers–Moyal-like expansion for the turbulent scalar flux as done by Kraichnan (1987) and Hamba (1995, 2004):

$$-\langle v'Y'_H\rangle(y,t) = D^{00}(y,t)\,\frac{\partial\langle Y_H\rangle}{\partial y} + D^{10}(y,t)\,\frac{\partial^2\langle Y_H\rangle}{\partial y^2} + D^{01}(y,t)\,\frac{\partial^2\langle Y_H\rangle}{\partial t\partial y} + D^{20}(y,t)\,\frac{\partial^3\langle Y_H\rangle}{\partial y^3} + \cdots, \tag{3.6}$$

$$D^{00}(y,t) = \iint D(y,y',t,t')\,\mathrm{d}y'\,\mathrm{d}t', \tag{3.7}$$

$$D^{10}(y,t) = \iint (y'-y)\,D(y,y',t,t')\,\mathrm{d}y'\,\mathrm{d}t', \tag{3.8}$$

$$D^{01}(y,t) = \iint (t'-t)\,D(y,y',t,t')\,\mathrm{d}y'\,\mathrm{d}t', \tag{3.9}$$

$$D^{20}(y,t) = \iint \frac{(y'-y)^2}{2}\,D(y,y',t,t')\,\mathrm{d}y'\,\mathrm{d}t'. \tag{3.10}$$

Here, D^{mn} are the eddy diffusivity moments; the first index, m, denotes order in space, while the second, n, denotes order in time. This is the form presented in Mani & Park (2021) and Liu, Williams & Mani (2023).

When the eddy diffusivity kernel is purely local,

$$D(y,y',t,t') = D^{00}\,\delta(y-y')\,\delta(t-t'). \tag{3.11}$$

In this case, D^{00} is the only surviving moment, while all higher-order moments in space and time are zero. Any non-zero higher-order moment therefore characterizes the non-locality of the eddy diffusivity kernel. Thus this expansion implies explicitly a model form for the turbulent scalar flux that incorporates non-locality of the eddy diffusivity. Truncating the expansion provides an approximation of $\langle v'Y'_H\rangle$, but with the caveat that the expansion may not converge. This will be discussed in more detail in § 5.3.1.

Each D^{mn} provides more information about the eddy diffusivity kernel with increasing order. For example, D^{00} represents the volume of the kernel in space–time. The coefficient corresponding to one higher order in space, D^{10}, provides information about the centroid of the kernel in space. Then D^{20} contains information about the moment of inertia of the kernel in space, D^{01} contains information about the centroid of the kernel in time, and so on.

3.3. *The macroscopic forcing method*

MFM is a method for numerically determining closure operators in turbulent flows (Mani & Park 2021). Much like a rheometer measures the molecular viscosity of a fluid by imposing a shear force on the flow, MFM forces the transport equation in a turbulent flow and extracts the closure operator from its response. Unlike the molecular viscosity, which is a material property, the turbulent closure operator is a property of the flow, so MFM measurements of one flow cannot be generalized for all flows; the MFM-measured closure for one flow cannot be applied exactly as it is to a different flow. However, MFM

https://doi.org/10.1017/jfm.2024.323 Published online by Cambridge University Press

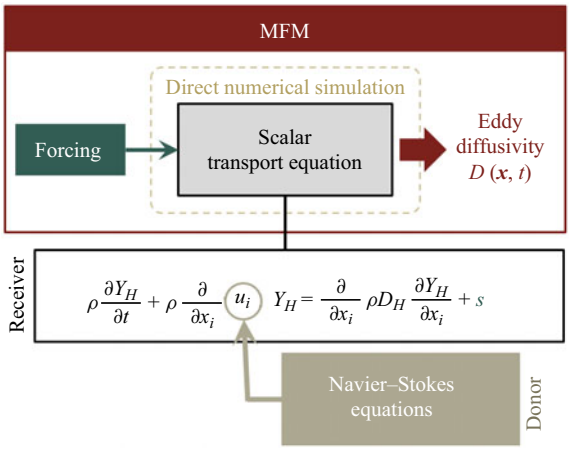

Figure 1. Diagram of the MFM pipeline.

measurements of one flow can reveal characteristics of the turbulent closure that are expected be true for a family of similar flows.

Specifically, MFM can be used to determine the RANS closure operator, as shown in the pipeline diagram in figure 1. In MFM, two simulations are run at once: the donor and receiver simulations. In this work, the donor simulation numerically solves the multicomponent Navier–Stokes equations in (4.1)–(4.4). The receiver simulation 'receives' u_i from the donor simulation, and uses it to solve the scalar transport equation with a forcing s:

$$\rho\frac{\partial Y_H}{\partial t} + \rho\frac{\partial}{\partial x_i}(u_i Y_H) = \frac{\partial}{\partial x_i}\left(\rho D_H\frac{\partial}{\partial x_i}Y_H\right) + s. \tag{3.12}$$

Ultimately, forcings on the receiver simulation effect a response from the flow, and measuring this response allows for determination of the eddy diffusivity. In particular, these forcings are macroscopic. Here, macroscopic quantities are defined as fields that are unchanged by Reynolds averaging. Mathematically, the macroscopic forcing is such that $s = \bar{s}$. This macroscopic nature is crucial to the method, since it does not disturb the underlying mixing process, which allows for measurement of the closure operator without changing it. For details, see Mani & Park (2021).

In actuality, the inverse MFM is used to determine eddy diffusivity moments. That is, instead of the forcings being chosen, certain mean mass fraction fields are chosen. Numerically, mean mass fractions are enforced in each realization, so the averages (denoted by $\bar{*}$) described here are in x, the homogeneous direction in space. The forcing needed to maintain the chosen $\overline{Y_H}$ is determined implicitly along the process, and is not used directly in the analysis.

As an illustration, the measurement of D^{00} can be considered. According to (3.6), choosing $\overline{Y_H} = y$ (for y between $-1/2$ and $1/2$) results in $\partial\overline{Y_H}/\partial y = 1$, and all other higher-order derivatives are zero. Thus choosing this $\overline{Y_H}$ in each realization results in the realization-averaged and spatially averaged measurement $-\langle v' Y_H'\rangle = D^{00}$.

Measurement of higher-order moments involves similar choices of $\overline{Y_H}$ but requires information from lower-order moments. For example, measuring D^{10} involves choosing $\overline{Y_H} = y^2$, which results in $-\langle v' Y_H'\rangle = yD^{00} + D^{10}$. Here, D^{00} comes from the simulation

https://doi.org/10.1017/jfm.2024.323 Published online by Cambridge University Press

using $\overline{Y_H} = y$. Thus D^{10} is computed by subtracting yD^{00} from the $\langle v'Y'_H\rangle$ measurement from the simulation using $\overline{Y_H} = y^2$.

Specifically, the following desired mean mass fractions are used for each moment for y between $-1/2$ and $1/2$:

$$\overline{Y_H} = y \Rightarrow D^{00}, \tag{3.13}$$

$$\overline{Y_H} = \tfrac{1}{2}y^2 \Rightarrow D^{10}, \tag{3.14}$$

$$\overline{Y_H} = yt \Rightarrow D^{01}, \tag{3.15}$$

$$\overline{Y_H} = \tfrac{1}{6}y^3 + \tfrac{1}{48} \Rightarrow D^{20}. \tag{3.16}$$

From these $\overline{Y_H}$, the needed forcing in each time step is determined numerically:

$$s^k = \frac{\overline{Y}^k_{H\,desired} - \overline{Y}^{k-1}_H}{\Delta t}, \tag{3.17}$$

where the superscript k denotes the time step number, $\overline{Y_{H\,desired}}$ is the mean mass fraction desired as outlined in (3.13)–(3.16), and Δt is the time step size.

This MFM forcing bears some resemblance to other forcings used in the literature, such as interaction by exchange with the mean (IEM) (Pope 2001; Sawford 2004). One main difference between forcings in such methods and MFM is that the purpose of the latter is to drive the flow to a specified mean gradient, which allows for measurement – not enforcement – of the eddy diffusivity moments. In other words, in MFM for scalar transport, the input is a mean scalar gradient, and the output is the eddy diffusivity moment; in IEM and similar methods, the input is a desired moment (e.g. in IEM, the input moment is $\langle c^2\rangle$) and the output is a mixing model. In addition, methods such as IEM use microscopic forcings, while MFM uses macroscopic forcings, which is a distinguishing characteristic of the latter method.

To determine D^{00}, D^{10}, D^{01} and D^{20}, four separate simulations are needed. For each of these simulations, the moments can be calculated using measurements of the turbulent scalar flux as follows:

$$D^{00} = F^{00}, \tag{3.18}$$

$$D^{10} = F^{10} - yD^{00}, \tag{3.19}$$

$$D^{01} = F^{01} - tD^{00}, \tag{3.20}$$

$$D^{20} = F^{20} - yD^{10} - \tfrac{1}{2}y^2D^{00}, \tag{3.21}$$

where F^{mn} denotes the $-\langle v'Y'_H\rangle$ measured from the receiver simulation using the forcing corresponding to the moment D^{mn}.

3.4. *Self-similarity analysis*

We perform our analysis in the self-similar regime. First, we define a self-similar coordinate:

$$\eta = \frac{y}{h(t)}, \tag{3.22}$$

so that $\langle Y_H\rangle$ is a function of only η. Note that η requires a definition of $h(t)$. From the previous discussion on the self-similarity of RTI, an appropriate definition is $h(t) = \alpha Agt^2$.

https://doi.org/10.1017/jfm.2024.323 Published online by Cambridge University Press

Through self-similar analysis of (3.6), the eddy diffusivity moments and turbulent scalar flux can be normalized. Details of this process can be found in Appendix A.

3.5. *Algebraic fit to mixing width*

Recall that $h(t) = \alpha A g t^2$ is used in the self-similarity analysis. This is valid only for late time, so the subsequent analyses in this work are all done in this self-similar time frame. Usually, α can be determined from $h(t)/Agt^2$, where $h(t)$ is computed from the simulation via (2.5). However, due to the convergence and statistical errors as well as the existence of a virtual time origin, $\alpha A g t^2$ is not a good representation of $h(t)$ measured in the DNS. Instead, a fitting coefficient α^* and virtual time origin t^* are determined to make a shifted quadratic fit to $h(t)$ from the simulation:

$$h_{fit}(t) = \alpha^* A g (t - t^*)^2. \tag{3.23}$$

With this fit, the normalizations of the turbulent scalar flux and moments become

$$\widehat{\langle v' Y'_H \rangle} = \frac{\langle v' Y'_H \rangle}{\alpha^* A g (t - t^*)}, \tag{3.24}$$

$$\widehat{D^{00}} = \frac{D^{00}}{\alpha^{*2} A^2 g^2 (t - t^*)^3}, \tag{3.25}$$

$$\widehat{D^{10}} = \frac{D^{10}}{\alpha^{*3} A^3 g^3 (t - t^*)^5}, \tag{3.26}$$

$$\widehat{D^{01}} = \frac{D^{01}}{\alpha^{*2} A^2 g^2 (t - t^*)^4}, \tag{3.27}$$

$$\widehat{D^{20}} = \frac{D^{20}}{\alpha^{*4} A^4 g^4 (t - t^*)^7}. \tag{3.28}$$

For exact self-similarity, plots of the measured $\widehat{D^{mn}}$ against η must be independent of time. This expectation sets a criterion to assess the extent to which ideal self-similarity is achieved. Plots and assessment of the self-similar collapse of the measurements presented in this work are in Appendix A.

4. Simulation details

4.1. *Governing equations*

The governing equations solved in this work are the compressible multicomponent Navier–Stokes equations, which involve equations for continuity, diffusion of mass fraction Y_α of species α (characterized by its binary molecular diffusivity D_α), momentum

https://doi.org/10.1017/jfm.2024.323 Published online by Cambridge University Press

transport, and transport of specific internal energy e:

$$\frac{\mathrm{D}\rho}{\mathrm{D}t} = -\rho \frac{\partial u_i}{\partial x_i}, \tag{4.1}$$

$$\rho \frac{\mathrm{D}Y_\alpha}{\mathrm{D}t} = \frac{\partial}{\partial x_i}\left(\rho D_\alpha \frac{\partial Y_\alpha}{\partial x_i}\right), \tag{4.2}$$

$$\rho \frac{\mathrm{D}u_j}{\mathrm{D}t} = -\frac{\partial}{\partial x_i}\left(p\delta_{ij} + \sigma_{ij}\right) + \rho g_j, \tag{4.3}$$

$$\rho \frac{\mathrm{D}e}{\mathrm{D}t} = -p \frac{\partial u_i}{\partial x_i} + \frac{\partial}{\partial x_i}\left(u_i\sigma_{ij} - q_j\right). \tag{4.4}$$

Here, $\mathrm{D}/\mathrm{D}t$ is the material derivative $\partial/\partial t + u_i(\partial/\partial x_i)$, ρ is density, u is velocity, p is pressure, and g is gravitational acceleration, active in the $-y$ direction. The viscous stress tensor σ_{ij} and heat flux vector q_j are respectively defined as

$$\sigma_{ij} = \mu\left(\frac{\partial u_i}{\partial x_j} + \frac{\partial u_j}{\partial x_i}\right) - \mu\,\frac{2}{3}\,\frac{\partial u_k}{\partial x_k}\,\delta_{ij}, \tag{4.5}$$

$$q_j = -\kappa \frac{\partial T}{\partial x_j} - \sum_{\alpha=1}^{N} h_\alpha \rho D_\alpha \frac{\partial Y_\alpha}{\partial x_j}. \tag{4.6}$$

Here, μ is the dynamic viscosity, κ is the thermal conductivity, T is temperature, and h_α is the specific enthalpy of species α.

Component pressures and temperatures of each species are determined using ideal gas equations of state. Under the assumption of pressure and temperature equilibrium, an iterative process is performed to determine volume fractions v_α that allow for computation of partial densities and energies. More details on the hydrodynamics equations and computation of component quantities can be found in Morgan *et al.* (2018).

Finally, total pressure is determined as the weighted sum of component pressures:

$$p = \sum_{\alpha=1}^{N} v_\alpha p_\alpha. \tag{4.7}$$

In general, in these compressible equations, Y_α are not passive scalars. However, the component equations of state are scaled so that a consistent hydrostatic pressure gradient is maintained across the mixing layer. Thus, in this work, Y_α are effectively passive.

4.2. *Computational approach*

Simulations for 2-D RTI are run using the Ares code, a hydrodynamics solver developed at Lawrence Livermore National Laboratory (Morgan & Greenough 2015; Bender *et al.* 2021). Ares employs an arbitrary Lagrangian–Eulerian method based on the one by Sharp & Barton (1981), in which the governing equations ((4.1)–(4.4)) are solved in a Lagrangian frame and then remapped to an Eulerian mesh through a second-order scheme. The spatial discretization is a second-order non-dissipative finite element method, and time advancement is a second-order explicit predictor–corrector scheme.

https://doi.org/10.1017/jfm.2024.323 Published online by Cambridge University Press

The Reynolds number (more specifically, the kinematic viscosity ν) is set through a numerical Grashof number, such that

$$\nu = \sqrt{\frac{-2gA\Delta^3}{Gr}}. \tag{4.8}$$

Here, Δ is the grid spacing; in the simulations, a uniform mesh is used, and $\Delta = \Delta x = \Delta y$. To ensure that the unsteady structures are properly resolved and for the simulation to appropriately be considered DNS, Gr should be kept small. A Gr that is too large results in a simulation with dissipation dominated by numerics rather than the physics. Morgan & Black (2020) found that past $Gr \approx 12$ in the Ares code, numerical diffusivity dominates molecular diffusivity. For our simulations, we use $A = 0.05$ and $Gr = 1$, the latter of which is in line with the DNS by Cabot & Cook (2006). These choices give $\nu = 10^{-9}\,\mathrm{m^2\,s^{-1}}$. The Schmidt number Sc, defined as ν/D_M, is set to unity, so $D_M = 10^{-9}\,\mathrm{m^2\,s^{-1}}$.

The Mach number $Ma = u/c$, where c is the speed of sound, characterizes compressibility effects of the flow, and is set by the specific heat ratio γ, which is 5/3 in the simulations in this work. The maximum Ma is measured at the last time step to be approximately 0.03, which is ascertained to be small enough to assume incompressibility.

The Péclet number Pe characterizes the advection versus diffusion rate and is defined as $Re\,Sc$. Here, Pe_L and Pe_T are reported, which use a large-scale Re_L and the Taylor Reynolds number Re_T, respectively. In the presented simulations, $Sc = 1$. The two Pe values are computed in post-processing: Pe_L is approximately 8000, and Pe_T is approximately 54. Both are below the criterion established by Dimotakis (2000), suggesting that the simulated flow is transitional or pre-transitional.

The number of cells in each simulation is 2049×2049. The width L_x of the domain is 1, and the height L_y is 1. The boundary conditions are periodic in x and no slip and no penetration in y.

Initially, the velocity field is zero, temperature is 293.15 K, and pressure is 1 atm. A top-hat perturbation based on the ones used by Morgan & Greenough (2015) and Morgan (2022) is imposed on the density field at the interface of the heavy and light fluids:

$$\xi(x) = \sum_{k=\kappa_{min}}^{\kappa_{max}} \frac{\Delta}{\kappa_{max} - \kappa_{min} + 1} \left(\cos\left(2\pi kx + \phi_{1,k}\right) + \sin\left(2\pi kx + \phi_{2,k}\right)\right), \tag{4.9}$$

$$\rho(x, y) = \rho_L + \frac{\rho_H - \rho_L}{2}\left(1 + \tanh\left(\frac{y - L_y/2 + \xi}{2\Delta}\right)\right), \tag{4.10}$$

where $\phi_{1,k}$ and $\phi_{2,k}$ are phase shift vectors taken randomly from a uniform distribution, and L_y is the length in y of the domain. Here, the minimum and maximum wavenumbers are set to $\kappa_{min} = 8$ and $\kappa_{max} = 256$, respectively.

The stop condition of the simulations is when h is approximately half the domain size in y. This corresponds to the non-dimensional simulation time τ of 30.84. Here, τ is defined as t/t_0, where $t_0 = \sqrt{h_0/Ag}$, and h_0 is the dominant length scale determined by the peak of the initial perturbation spectrum.

Before MFM analysis was conducted, the results of the donor simulations were examined. In figure 2(*a*), mixedness is observed to reach a value of approximately 0.6, but appears not to have converged yet. Figure 2(*b*) shows the two definitions of α over time. The first definition, $\alpha = h/Agt^2$, reaches a value of about 0.05 by the end of the simulation,

https://doi.org/10.1017/jfm.2024.323 Published online by Cambridge University Press

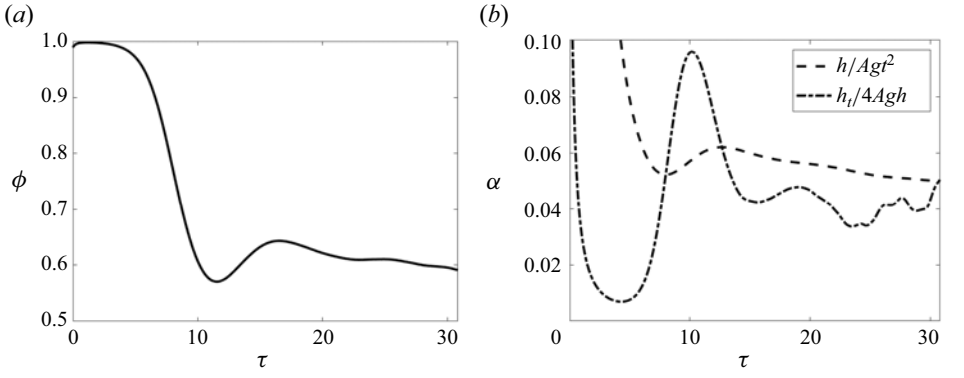

Figure 2. Self-similarity parameters computed from a donor simulation.

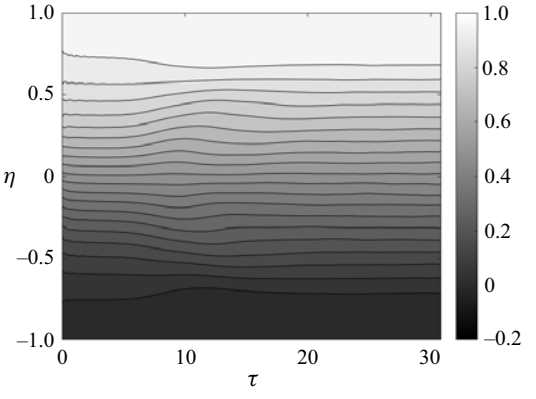

Figure 3. Contours of $\langle Y_H \rangle$ showing self-similarity at late times.

but it does not appear to be converged. The second definition, $\alpha = \dot{h}^2/4Agh$, is oscillatory, due to the sensitivity of the time derivative to noise, and it appears to fluctuate about a value of approximately 0.04. It is acknowledged that this behaviour indicates that the RTI simulated here is only weakly turbulent. However, it is observed that the flow is still self-similar at late times. The contour plot of $\langle Y_H \rangle$ in figure 3 exhibits parallel contour lines after $\tau \approx 17$, indicating self-similarity at those times. It is also shown in Appendix A that the mean concentration and normalized turbulent scalar flux profiles exhibit self-similar collapse after $\tau \approx 17$, so the presented self-similar analysis is valid.

Figure 4 shows a plot of the algebraic fit for h, described in (3.23). For the simulations presented here, α^* is 0.0046, and t^* is -1.6×10^3. The plot shows a strong quadratic dependence of h on t at late time, as h_{fit} matches DNS at $\tau \gtrapprox 17$, validating the self-similar ansatz of $h \sim t^2$.

To further ensure that the simulations are working as desired, the flow fields of the donor and receiver simulations can be examined qualitatively. The Y_H contours at the last time steps of each simulation are shown in figure 5. The receiver simulation shown is the one used to compute D^{00} (where $\langle Y_H \rangle = y$). Self-similar RTI turbulent mixing is observed at this time step, where the characteristic heavy spikes are sinking into the lighter fluid, and the light bubbles rise into the heavier fluid. Both simulations have the same velocity fields, since the receiver simulation 'receives' the velocity field from the donor simulation.

https://doi.org/10.1017/jfm.2024.323 Published online by Cambridge University Press

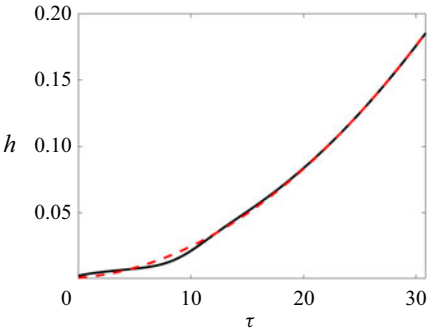

Figure 4. Black solid line indicates h measured from DNS; red dashed line indicates h_{fit}.

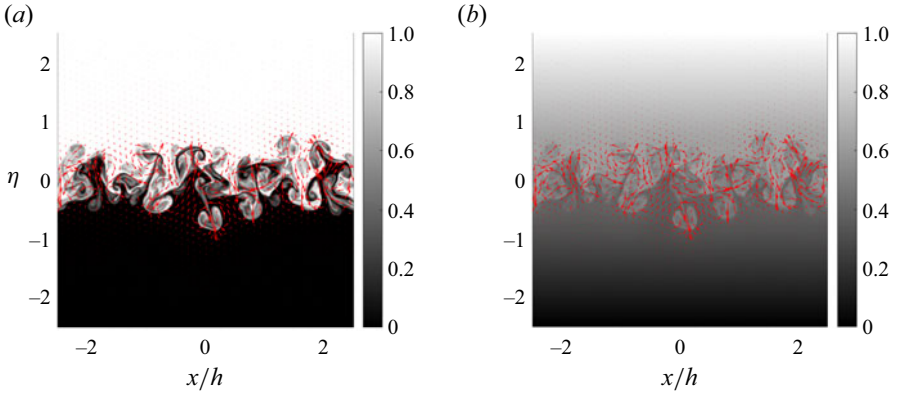

Figure 5. Contours of Y_H (black indicates light, white indicates heavy) and velocity vector fields (red arrows) for (a) the donor simulation and (b) the receiver simulation with s enforcing $\langle Y_H \rangle = y$. These snapshots are taken at the last time step.

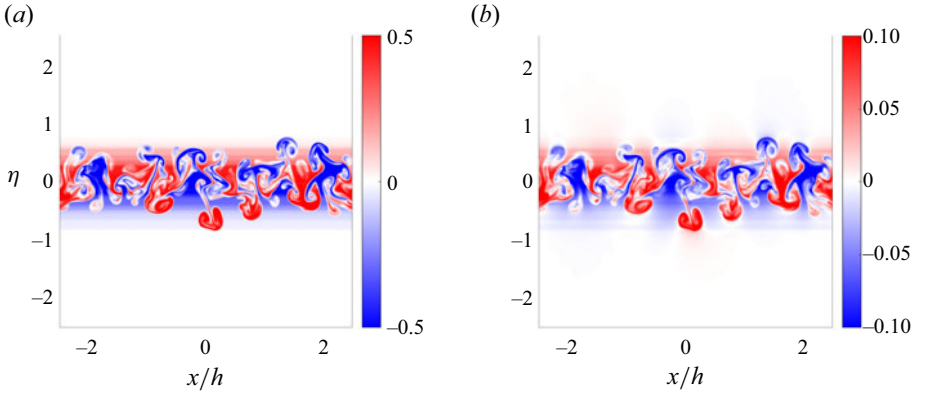

Figure 6. Contours of Y'_H for (a) the donor simulation and (b) the receiver simulation. These snapshots are taken at the last time step. Note that different colour bars have been used to improve interpretability.

In contrast with the donor simulation, which has a stark black-and-white difference between the heavy and light fluids, there is a grey gradient of density in the receiver simulation due to the imposed mean scalar gradient. The fluctuations of Y_H in each simulation are also compared in figure 6. The Y'_H contours are not identical but are

https://doi.org/10.1017/jfm.2024.323 Published online by Cambridge University Press

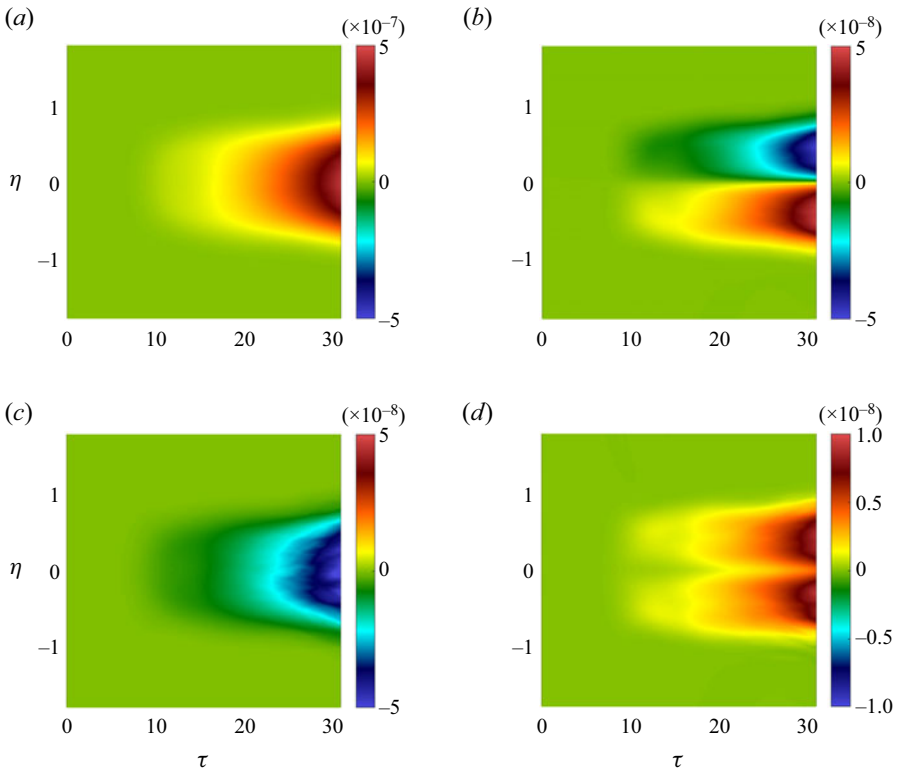

Figure 7. Moments of eddy diffusivity kernel normalized by appropriate length and time scales. Data averaged over 1000 realizations and homogeneous direction x, for (*a*) D^{00}, (*b*) $D^{10}/h(t)$, (*c*) D^{01}/t, (*d*) $D^{20}/h(t)^2$.

qualitatively very similar. In both simulations, Y'_H is constrained to the mixing layer. Based on these observations, it is concluded that the simulations are visually working as intended.

5. Results

5.1. *Eddy diffusivity moments*

Figure 7 shows normalized MFM measurements of the eddy diffusivity moments D^{00}, D^{10}, D^{01} and D^{20} averaged over 1000 realizations and the homogeneous direction x. Some expected characteristics of the measured moments are observed.

(i) The leading-order moment is over two magnitudes larger than the molecular diffusivity (10^{-9} m^2 s^{-1}). The scaled higher-order moments shown are all at least one magnitude larger than the molecular diffusivity.

(ii) Here, D^{00} is symmetric and always positive.

(iii) Here, D^{10} is antisymmetric. This antisymmetry can be understood by interpreting D^{10}/D^{00} as the centroid of the eddy diffusivity kernel. Physically, for $\eta > 0$, it is expected that the mean scalar gradient at the centre of the mixing layer (at a negative distance away) has more influence on the turbulent scalar flux than the mean scalar gradient at the outer edges, since the mixing layer is growing outwards. This makes the eddy diffusivity kernel skewed more towards the centre of the

https://doi.org/10.1017/jfm.2024.323 Published online by Cambridge University Press

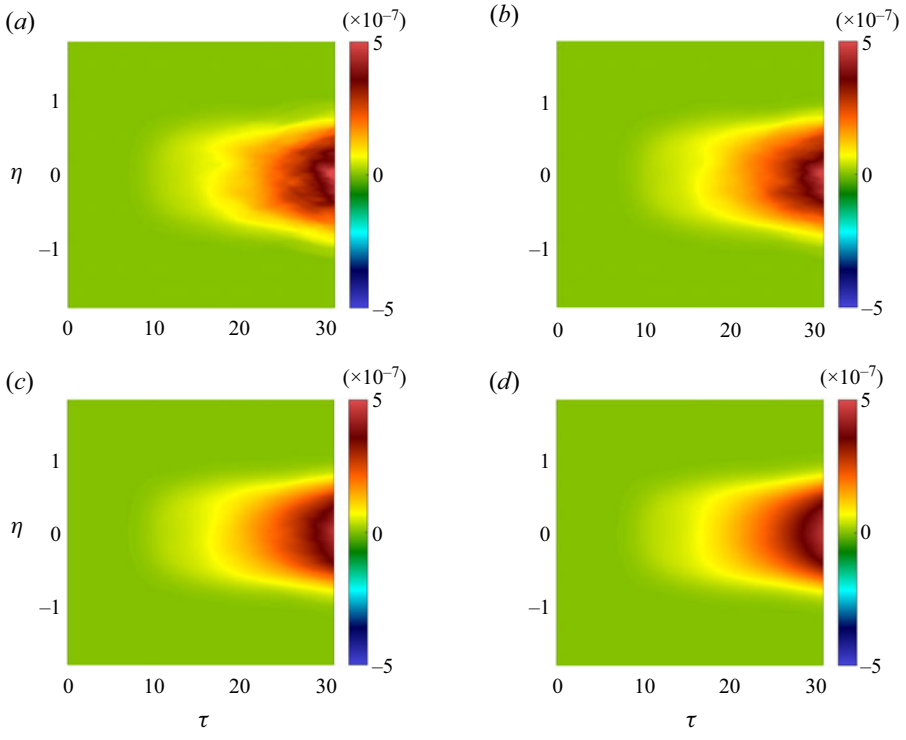

Figure 8. Moment D^{00} averaged over different numbers of realizations: (*a*) 8, (*b*) 32, (*c*) 100, (*d*) 1000.

domain, so $D^{10} < 0$ for $\eta > 0$. A similar effect occurs for $\eta < 0$, which results in $D^{10} > 0$.

(iv) Here, D^{01} is symmetric and always negative. The latter must be true for the flow to depend on its history (it does not violate causality).

(v) Here, D^{20} is symmetric and always positive, as is characteristic of moment of inertia of a positive kernel.

Based on the magnitudes of the normalized moments, some initial observations on the importance of each moment can be made. Here, D^{00} has the highest magnitude of all the moments, which is expected since it is the leading-order moment. The magnitudes of D^{10}/h and D^{01}/t are of the order of 10 % of the magnitude of D^{00}, which suggests that they are non-negligible. On the other hand, the magnitude of D^{20}/h^2 is of the order of 1 % of that of D^{00}, so D^{20} is likely not an important moment to include in modelling RTI. More robust studies will be presented in the following subsections to determine the importance of each of the eddy diffusivity moments.

It is also observed that there is statistical error in the measurements. Due to the chaotic nature of RTI, the moment measurements contain statistical error, but this error can be reduced by averaging many realizations. To demonstrate statistical convergence of the measurements, plots of D^{00} averaged over different numbers of realizations are included in figure 8. As the number of realizations increases, the plots become smoother, and it is found that after 1000 realizations, the rate of reduction in statistical error slows down significantly. Averaging over this number of realizations results in a smooth D^{00}

https://doi.org/10.1017/jfm.2024.323 Published online by Cambridge University Press

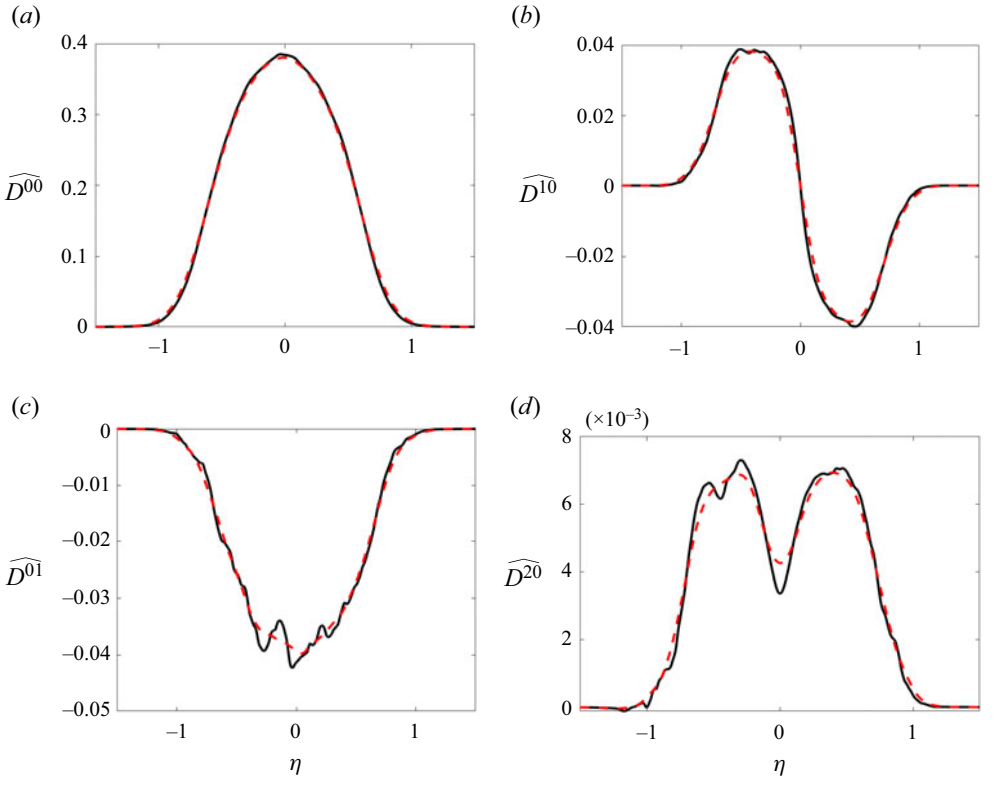

Figure 9. Smoothed moments (dashed red) over raw MFM measurements of moments (solid black). The moments are taken from the mean data at the last time step of the simulations and are transformed to self-similar space.

measurement and higher-order moment measurements with acceptably less statistical error.

Additionally, the higher the order of the moment, the slower its rate of statistical convergence. Recall that determination of higher-order moments requires information from lower-order moments. For example, in determining D^{01}, tD^{00} is subtracted from F^{01}, the turbulent scalar flux measurement in the simulation associated with D^{01}. Naturally, there is statistical error associated with both D^{01} and D^{00}. However, the error in D^{00} is amplified by t, so the overall statistical error of D^{01} increases with time. This statistical error 'leakage' occurs for all higher-order moments. The higher the order of the moment, the worse the statistical error, since information from more lower-order moments is needed, so more statistical error is accumulated and amplified. The relatively high statistical error of the higher-order moments makes it challenging to study their importance. In particular, taking derivatives of quantities with high statistical error amplifies the error, so smoother measurements are desired. In this work, the moment measurements are smoothed using a Savitzky–Golay filter function in Matlab with a polynomial order of unity and window size 191. These smoothed moments are shown in figure 9. While it is possible to design an alternative formulation of the MFM that removes leakage of statistical error from low-order moments to higher-order moments (see Lavacot *et al.* 2022), for this 2-D study and for the order of moments considered here, the statistical convergence is sufficient.

https://doi.org/10.1017/jfm.2024.323 Published online by Cambridge University Press

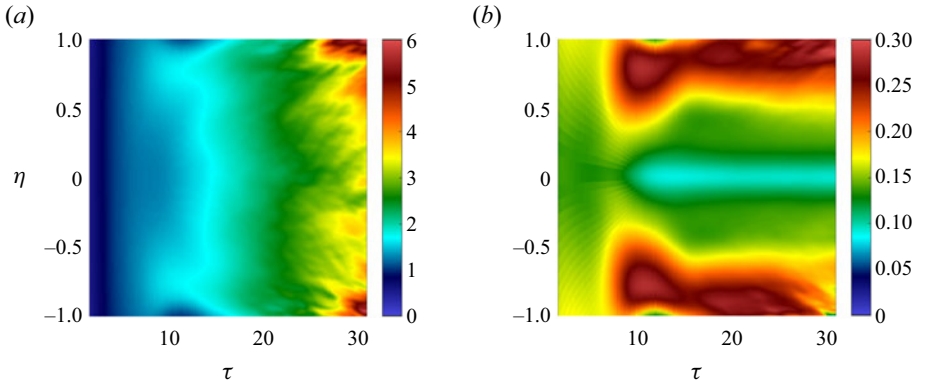

Figure 10. Non-dimensional non-local time scale and length scale contours: (*a*) τ_{NL}, (*b*) η_{NL}. Only $-1 \leq \eta \leq 1$ is plotted, since moments are zero outside the mixing layer. Early times ($\tau < 2$) are not plotted due to transient behaviour.

Using these measurements, non-local time scales and length scales (t_{NL} and L_{NL}, respectively) can be defined:

$$t_{NL} = -\frac{D^{01}}{D^{00}}, \quad L_{NL} = \sqrt{\frac{D^{20}}{D^{00}}}. \tag{5.1a,b}$$

Note that this analysis can be done only for $-1 \leq \eta \leq 1$, since the moments are analytically zero outside the mixing layer.

Non-dimensionally, the non-local time scale is $\tau_{NL} = t_{NL}/t_0$, and the non-local length scale is $\eta_{NL} = L_{NL}/h$. Contour plots of the non-dimensionalized non-local time scale and length scale are in figure 10. Note that τ_{NL} scales as τ, so profiles of τ_{NL}/τ against η are also plotted in figure 11 in the self-similar time regime ($\tau > 17$). The scaled profiles collapse and have centreline value approximately 0.1. This means that the mean fluxes at some time τ are affected by mean scalar gradients 0.1τ earlier. Figure 12 shows that the minimum non-local length scale is at the centreline, where $\eta_{NL} \approx 0.09$. The maximum length scales occur near the outer edges of the mixing layer: at approximately $\eta = \pm 0.87$, $\eta_{NL} \approx 0.27$. This indicates that mean fluxes at the mixing layer edges depend mostly on mean scalar gradients approximately a quarter of a mixing width away, while mean fluxes at the centreline depend on mean scalar gradients approximately one-tenth of a mixing width away; non-locality appears to be stronger at the mixing layer edges than at the centreline. These non-local properties of the eddy diffusivity for RTI could not be predicted without direct measurement of the eddy diffusivity moments, which has been made possible through MFM.

5.2. *Assessment of importance of non-local effects*

5.2.1. *Comparison of terms in the turbulent scalar flux expansion*

To aid in the determination of which moments are important for a RANS model, a comparison of the terms in the expansion of the turbulent scalar flux (3.6) is presented. These terms involve gradients of $\langle Y_H \rangle$. Instead of using $\langle Y_H \rangle$ directly from the DNS, a fit to $\langle Y_H \rangle$ is used, since the statistical error in the raw measurement gets amplified by derivatives in η. That is, the quantities of interest are sufficiently converged for plotting

https://doi.org/10.1017/jfm.2024.323 Published online by Cambridge University Press

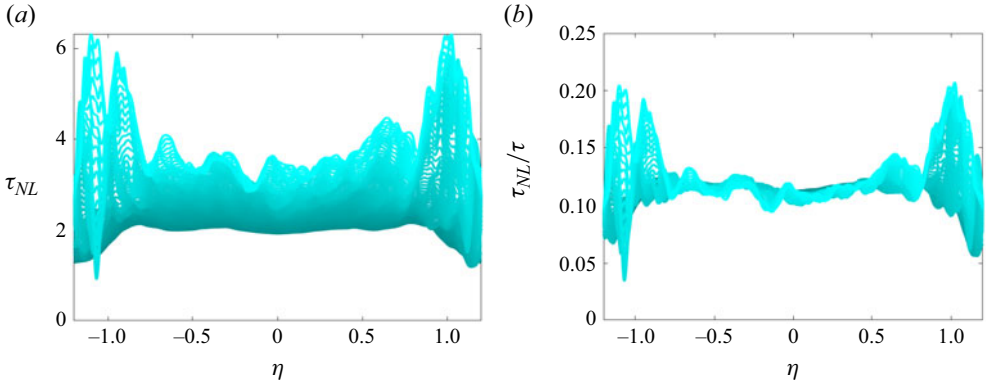

Figure 11. Non-dimensional non-local time scale profiles at different times for $\tau > 17$. Lighter lines correspond to later times; darker lines correspond to earlier times. (*a*) Unscaled, showing the linear time dependence of τ_{NL} on τ. (*b*) The collapse of the profiles when scaled by τ.

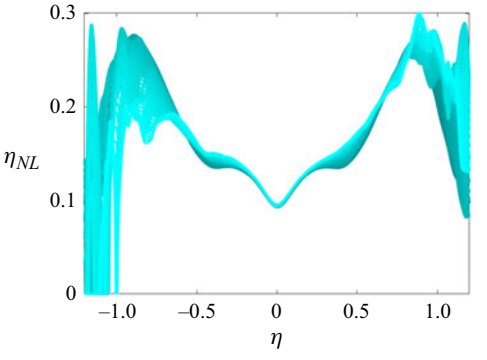

Figure 12. Non-dimensional non-local length scale profiles at different times for $\tau > 17$. Lighter lines correspond to later times; darker lines correspond to earlier times.

but not for operations involving derivatives. Thus an analytical fit to $\langle Y_H \rangle$ is obtained as follows:

$$\langle Y_H \rangle^* = \begin{cases} 0, & \text{if } \eta < -a, \\ \displaystyle\int_{-a}^{\eta} \frac{1}{(a^2 - \eta'^2)^2} \exp\left(\frac{1}{B(a^2 - \eta'^2)}\right) \mathrm{d}\eta', & \text{if } -a \le \eta \le a, \\ 1, & \text{if } \eta > a, \end{cases} \tag{5.2}$$

$$\langle Y_H \rangle = \frac{\langle Y_H \rangle^*}{\langle Y_H \rangle^*_{max}}, \tag{5.3}$$

where the integral is determined numerically, and a and B are fitting coefficients. The coefficients $a^2 = 1.2$ and $B = 0.36$ are found to give good agreement with the mean concentration profile from DNS, as shown in figure 13.

The terms on the right-hand side of (3.6) are plotted against the DNS measurement of the turbulent scalar flux in figure 14. Clearly, the $\widehat{D^{00}}$ term is not enough to capture the turbulent scalar flux. It is observed that the $\widehat{D^{01}}$ term is significant in magnitude in the middle of the domain, and the $\widehat{D^{10}}$ term carries importance at the outer edges of the mixing layer. The term associated with the highest-order moment that was measured, $\widehat{D^{20}}$, also appears to be of magnitude similar to the other moments, indicating that

https://doi.org/10.1017/jfm.2024.323 Published online by Cambridge University Press

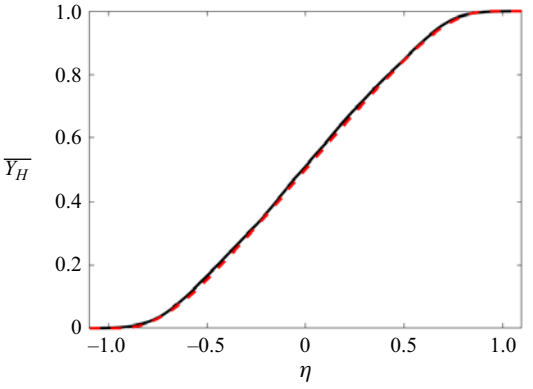

Figure 13. Semi-analytical fit to $\langle Y_H \rangle$ (dashed red) against DNS measurement of $\langle Y_H \rangle$ (solid black).

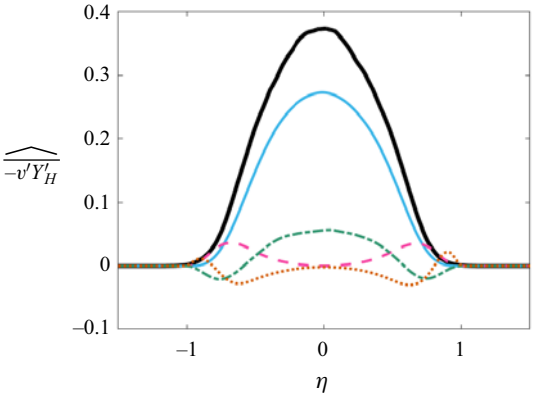

Figure 14. Comparison of terms in the expansion of the turbulent scalar flux. Solid black indicates DNS measurement of turbulent scalar flux; solid blue indicates the $\widehat{D^{00}}$ term; dashed pink indicates the $\widehat{D^{10}}$ term; dash-dotted green indicates the $\widehat{D^{01}}$ term; dotted orange indicates the $\widehat{D^{20}}$ term.

it may also carry important information about non-locality of the eddy diffusivity. These preliminary findings indicate that non-locality is certainly important for accurate modelling of mean scalar transport in this RTI problem, since the higher-order terms in (3.6) appear non-negligible compared to the leading-order term. It may be tempting to ascribe physical reasons for the behaviour of the terms plotted in figure 14, but this is not so straightforward, especially since the full eddy diffusivity kernel for this problem has not yet been measured. Further, it would be inappropriate to draw conclusions about importance of each eddy diffusivity moment in a RANS model, since the operator form must be scrutinized first. A faulty operator form could give misleading implications about certain eddy diffusivity moments. It turns out that a simple superposition of these terms, which would represent a truncation of (3.6), does not accurately represent the true eddy diffusivity kernel and actually leads to divergence of predictions, so such an operator form would not be appropriate; this will be covered more in depth in § 5.3. Nevertheless, the results shown here are strong evidence of non-locality of the eddy diffusivity kernel for the RTI simulated here.

https://doi.org/10.1017/jfm.2024.323 Published online by Cambridge University Press

5.2.2. *Comparison of the leading-order model against a local model*

To demonstrate the shortcomings of models using purely local coefficients, an MFM-based leading-order model and the k-L RANS model are compared. The intent of this study is not to immediately propose a 'better' RANS model to replace k-L, nor is it to suggest that the MFM-based leading-order model is more accurate than the k-L model. In fact, it is expected that the MFM-based leading-order model will perform poorly, since it does not include important higher-order moments of eddy diffusivity. Instead, this study emphasizes the necessity of higher-order moments, and shows how MFM can reveal incorrect model forms.

In particular, a one-dimensional k-L simulation is run, and the eddy diffusivity and mean concentration profiles are extracted from the results to be compared to those of the MFM-based model using the measured D^{00} that was presented in § 5.1. The k-L simulation used in this section is implemented in Ares, and details of the implementation are in Morgan & Greenough (2015) and Morgan (2018). Note that the k-L simulation is used here for illustration purposes and should not be confused with the 2-D DNS used to obtain our MFM moments.

The MFM-measured D^{00} is used for the leading-order MFM-based model:

$$-\langle v'Y_H'\rangle = D^{00}_{MFM}\,\frac{\partial\langle Y_H\rangle}{\partial y}. \tag{5.4}$$

To solve this, D^{00}_{MFM} is obtained from the smoothed MFM measurements and transformed to self-similar coordinates. The resulting $\widehat{D^{00}_{MFM}}$ is a function of $\eta = y/h_{DNS}$, where $h_{DNS} = \alpha^*_{DNS} A g (t - t^*_{DNS})^2$ is an algebraic fit to the mixing width from the DNS. The equation is then solved semi-analytically in conjunction with the mean mass fraction evolution equation in self-similar coordinates:

$$-2\eta\,\frac{\mathrm{d}\langle Y_H\rangle}{\mathrm{d}\eta} = \frac{\mathrm{d}}{\mathrm{d}\eta}\left(-\widehat{\langle v'Y_H'\rangle}\right), \tag{5.5}$$

$$-\widehat{\langle v'Y_H'\rangle} = \widehat{D^{00}_{MFM}}\,\frac{\mathrm{d}\langle Y_H\rangle}{\mathrm{d}\eta}. \tag{5.6}$$

The k-L model uses the gradient diffusion approximation for the turbulent flux:

$$-\langle v'Y_H'\rangle = \frac{\mu_t}{\langle\rho\rangle N_Y}\,\frac{\partial\langle Y_H\rangle}{\partial y} = D^{00}_{k\text{-}L}\,\frac{\partial\langle Y_H\rangle}{\partial y}, \tag{5.7}$$

where $\mu_t = C_\mu \langle\rho\rangle L\sqrt{2k}$, and N_Y is one of the model coefficients set by similarity constraints derived by Dimonte & Tipton (2006). In particular, this work uses the coefficient calibration detailed in (Morgan & Greenough 2015), and the coefficients are chosen to achieve the same α as the DNS. Here, C_μ is unity and N_Y is 2.47. The k-L RANS model is solved in spatio-temporal coordinates, and the $\langle\rho\rangle$, k and L obtained from the solution are used to compute μ_t and, consequently, $D^{00}_{k\text{-}L}$, which is purely local. For a meaningful comparison with the MFM-based model, $D^{00}_{k\text{-}L}$ is transformed to $\widehat{D^{00}_{k\text{-}L}}$ according to the self-similar coordinate $\xi = y/h_{k\text{-}L}$, where $h_{k\text{-}L} = \alpha^*_{k\text{-}L} A g (t - t^*_{k\text{-}L})^2$. It must be noted that the h fitting coefficients α^* and t^* are not the same between the DNS and k-L solutions. In this work, $\alpha^*_{DNS} = 0.046$, $t^*_{DNS} = -1600$ s, $\alpha^*_{k\text{-}L} = 0.04$ and $t^*_{k\text{-}L} = 1250$ s ($t^*_{k\text{-}L}$ is positive due to the relaxation time to the self-similar profiles in the beginning of the k-L simulation).

https://doi.org/10.1017/jfm.2024.323 Published online by Cambridge University Press

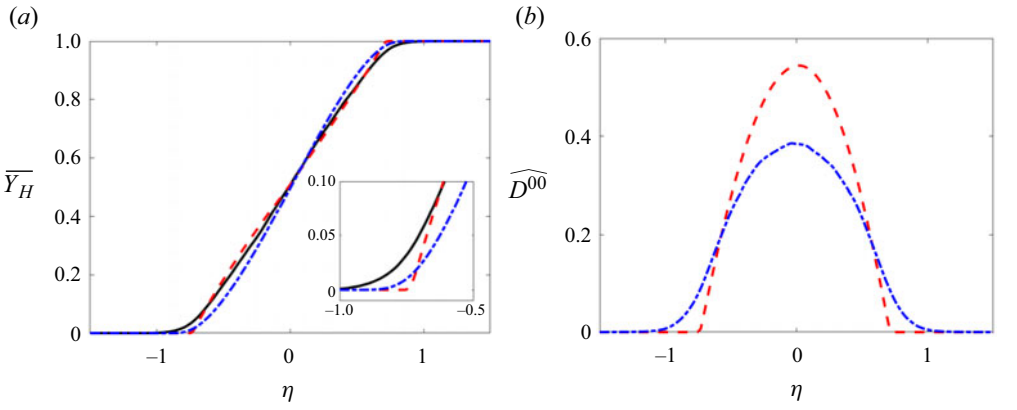

Figure 15. Comparisons of (*a*) model coefficient from the *k*-*L* model with leading-order moment measured using MFM, and (*b*) resulting similarity solutions for $\langle Y_H \rangle$. Inset in (*a*) shows zoomed-in view around $\eta = -1$ to highlight divergence of the *k*-*L* model from DNS. Solid black indicates DNS measurement; dash-dotted blue indicates leading-order MFM-based model; dashed red indicates the *k*-*L* model.

Figure 15(*a*) shows the mean concentration profiles computed using each of the two models. As expected, the MFM-based leading-order model performs poorly, not capturing the slope of the DNS profile, since that model uses only the leading-order eddy diffusivity moment and incorporates no information about non-locality of the eddy diffusivity. The *k*-*L* model exhibits divergence from DNS at the outer edges of the mixing layer, since it is designed to predict a linear $\langle Y_H \rangle$ profile. However, it does capture the slope of the DNS profile, despite it also using a leading-order closure. In addition, it is observed in figure 15(*b*) that the MFM-measured $\widehat{D^{00}_{MFM}}$ is significantly lower in magnitude than $\widehat{D^{00}_{k\text{-}L}}$. Here, MFM reveals that the *k*-*L* model is using an incorrect model form, since the D^{00} that it is using does not match the MFM measurement. In fact, the *k*-*L* model is using this higher-magnitude coefficient in order to compensate for the error in model form and achieve a linear mean concentration profile with a slope that matches the DNS. Despite this compensation, the *k*-*L* model still disagrees with the DNS results at the outer edges of the mixing layer, which are important for capturing the average reaction rate in reacting flows as in ICF. A more accurate RANS model would more closely match the eddy diffusivity moments measured by MFM. As results will show shortly, the gap between the leading-order MFM-based model $\langle Y_H \rangle$ and the DNS measurement would be bridged by inclusion of higher-order moments, which would introduce information about the non-locality of the eddy diffusivity.

5.3. *Assessment of non-local operator forms*

In this subsection, two RANS operator forms using information about the non-locality of the eddy diffusivity are presented. These are the explicit and implicit operator forms; the former is a truncation of the turbulent scalar flux expansion (3.6), and the latter will be presented shortly. It must be stressed that the intention of the following studies is not to propose a new RANS model. Ultimately, a RANS model should not depend on direct MFM measurements that can be retrieved only from impractically many DNS. Instead, these studies are performed to further assess the importance of each of the eddy diffusivity moments, determine which combinations of moments best enhance the performance of

https://doi.org/10.1017/jfm.2024.323 Published online by Cambridge University Press

a RANS model, and examine the differences between the explicit and implicit operator forms. The aim of these studies is to inform development of more predictive RANS models for RTI, not to suggest that these are the exact models that should be used.

In addition, D^{20} will not be included in the following studies. This is mainly due to the high statistical error in the measurement that makes it difficult to ascertain whether errors in the results are due to this statistical error or solely the addition of the moment to the model. From the comparison of terms in § 5.2.1, it is expected that D^{20} is not as important as D^{10} and D^{01} to include in a RANS model. This should be tested in future work when a more statistically converged measurement is achieved for D^{20}, ideally in a 3-D analysis.

5.3.1. *Explicit operator form*

The explicit operator form is a truncation of the expansion of the turbulent scalar flux, as defined in (3.6). Hamba (1995, 2004) has examined this form in the context of shear flows. Transformation of this expansion to self-similar coordinates and substitution into (3.3) results in

$$-2\eta \frac{\mathrm{d}\langle Y_H\rangle}{\mathrm{d}\eta} = \frac{\mathrm{d}}{\mathrm{d}\eta}\left[\left(\widehat{D^{00}} - \widehat{D^{01}}\right)\frac{\mathrm{d}\langle Y_H\rangle}{\mathrm{d}\eta} + \left(-\eta\widehat{D^{01}} + \widehat{D^{10}}\right)\frac{\mathrm{d}^2\langle Y_H\rangle}{\mathrm{d}\eta^2} + \widehat{D^{20}}\frac{\mathrm{d}^3\langle Y_H\rangle}{\mathrm{d}\eta^3} + \cdots\right], \tag{5.8}$$

which can be solved numerically for $\langle Y_H\rangle$. The $\widehat{D^{mn}}$ used in the numerical solve are the smoothed, normalized moments. To determine which eddy diffusivity moments are important in constructing RANS models for RTI, different combinations of $\widehat{D^{mn}}$ terms are kept in (5.8), and the results are compared to DNS. In the numerical solve, (5.8) is discretized on a staggered mesh, and derivatives are computed using central finite differences. A matrix–vector equation is assembled and solved for $\langle Y_H\rangle$ with Dirichlet boundary conditions.

Figure 16 shows the turbulent scalar fluxes computed using the explicit operator form, and figure 17 shows the corresponding mean concentration profiles. Again, it is apparent that the leading-order moment is not enough to capture the turbulent scalar flux. The combination using D^{00}, D^{10} and D^{01} – the moments deemed most important in § 5.2.1 – gives the best match to the DNS measurement.

It is particularly remarkable that a converged turbulent scalar flux can be obtained using D^{00}, D^{10} and D^{01}. As mentioned previously, it is known that (3.6) may not converge. That is, the expansion must be taken to infinite terms to remove error; truncating the expansion can result in significant error. This is analogous to a Kramers–Moyal expansion, which cannot be approximated adequately by more than two terms, after which it requires infinite terms for convergence (Pawula 1967; Mauri 1991). To understand how adding terms to (3.6) can result in greater error, one can consider the eddy diffusivity kernel associated with each term. The leading-order moment is associated with a delta function kernel, as it is purely local. However, when (3.4) is replaced by (3.6), an integral operator is replaced with a high-order differential operator. This means that the non-local effects are approximated by derivatives of delta functions; see Liu *et al.* (2023) for more details. It has been shown that in general, the eddy diffusivity kernel is not a superposition of finite delta functions, as it is smooth (Mani & Park 2021; Liu *et al.* 2023). Therefore, truncation of the expansion does not match the shape of the eddy diffusivity kernel, leading to errors in prediction of the turbulent scalar flux. While the D^{00}, D^{10} and D^{01} combination did not diverge, adding D^{20} does lead to divergent results for these reasons, so this combination is not presented here.

https://doi.org/10.1017/jfm.2024.323 Published online by Cambridge University Press

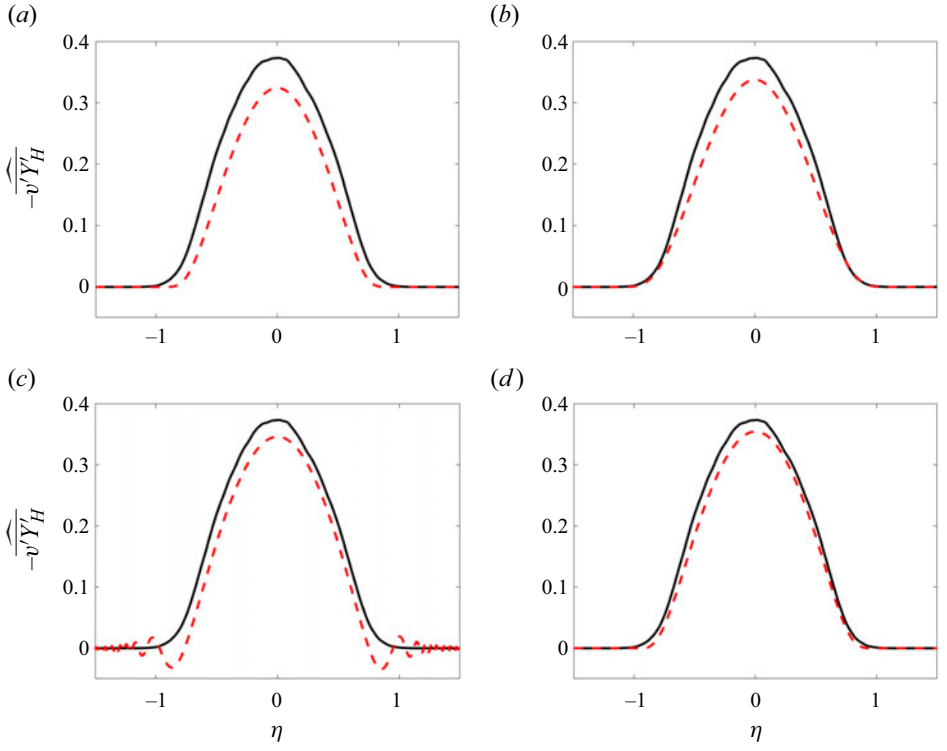

Figure 16. Turbulent scalar flux predictions using the explicit operator form. Moments used in the model are: (*a*) D^{00}; (*b*) D^{00}, D^{10}; (*c*) D^{00}, D^{01}; (*d*) D^{00}, D^{10}, D^{01}.

Another issue with the explicit operator form is its numerical implementation. In spatio-temporal space, some terms associated with higher-order moments involve mixed derivatives (e.g. the term $D^{01}(\partial^2/\partial t\,\partial y)$), which would undergo another spatial gradient when substituted into (3.3). Such terms are difficult to handle numerically. In this work, the model is implemented in the more convenient self-similar space, but ultimately, a spatio-temporal model would be developed, as it is more practical. It is thus pertinent to work towards a better method to incorporate non-local information in a RANS model that does not encounter the Kramers–Moyal-like convergence issue and is easier to implement.

5.3.2. *Implicit operator form and the matched moment inverse*

In this section, an implicit operator form is introduced as a solution to both the increasing error when adding terms from the turbulent scalar flux expansion and implementation challenges associated with the explicit operator form. Recall that the explicit operator form fails to match the shape of the eddy diffusivity kernel without infinite terms of the turbulent scalar flux expansion. In this implicit operator form, the aim is to match the shape of the eddy diffusivity kernel, instead of using the truncated expansion for the turbulent scalar flux. Using the four moments that have been measured, this model form is

$$\left[1 + a^{01}\frac{\partial}{\partial t} + a^{10}\frac{\partial}{\partial y} + a^{20}\frac{\partial^2}{\partial y^2} + \cdots\right](-\langle v'Y'_H\rangle) = a^{00}\frac{\partial\langle Y_H\rangle}{\partial y}, \tag{5.9}$$

where $a^{mn}(y,t)$ are model coefficients fitted corresponding to each of the eddy diffusivity moments D^{mn} measured using MFM. The bracketed operator on the left-hand side is the

https://doi.org/10.1017/jfm.2024.323 Published online by Cambridge University Press

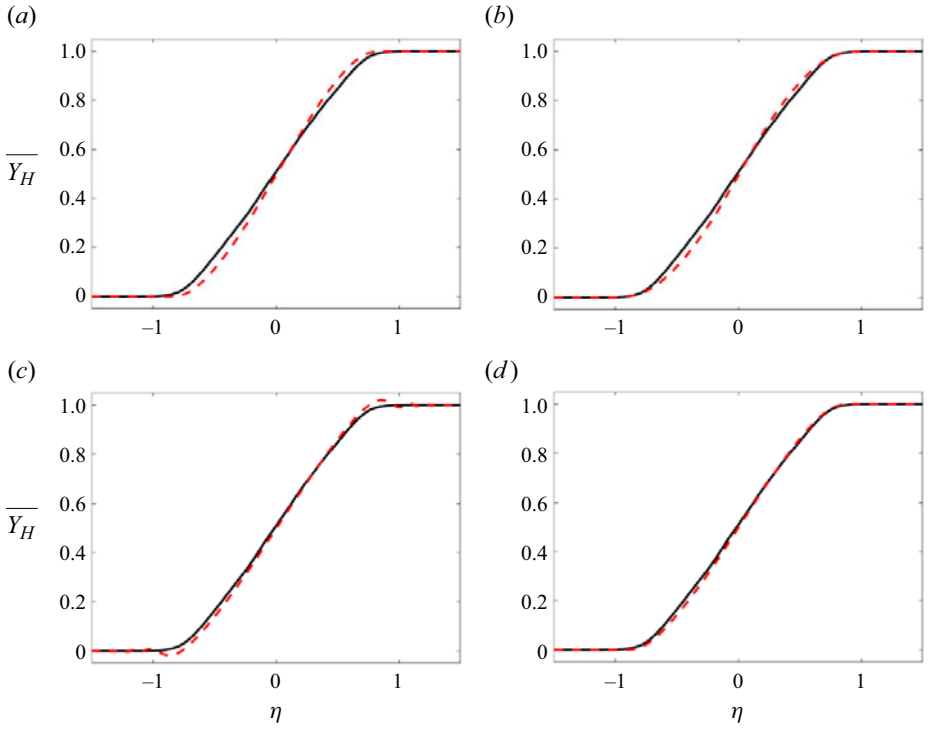

Figure 17. Mean concentration profile predictions using the explicit operator form. Moments used in the model are: (*a*) D^{00}; (*b*) D^{00}, D^{10}; (*c*) D^{00}, D^{01}; (*d*) D^{00}, D^{10}, D^{01}.

matched moment inverse (MMI) operator. The way this model form is designed to match the eddy diffusivity kernel shape is detailed in Liu *et al.* (2023). In addition, this form is significantly easier to implement numerically in spatio-temporal space, since it can be directly time-integrated using explicit methods. In this way, it is also easy to add more terms with higher-order moments, as it simply requires extension of the operator.

In self-similar coordinates, this becomes

$$\left[1+\widehat{a^{01}}\left(1-2\eta\,\frac{\mathrm{d}}{\mathrm{d}\eta}\right)+\widehat{a^{10}}\,\frac{\mathrm{d}}{\mathrm{d}\eta}+\widehat{a^{20}}\,\frac{\mathrm{d}^2}{\mathrm{d}\eta^2}+\cdots\right]\widehat{(-\langle v'Y'_H\rangle)}=\widehat{a^{00}}\,\frac{\mathrm{d}\langle Y_H\rangle}{\mathrm{d}\eta},\tag{5.10}$$

where it is found through self-similar analysis that

$$\widehat{a^{00}}=\frac{1}{\alpha^{*2}A^2g^2(t-t^*)^3}\,a^{00},\tag{5.11}$$

$$\widehat{a^{01}}=\frac{1}{t-t^*}\,a^{01},\tag{5.12}$$

$$\widehat{a^{10}}=\frac{1}{\alpha^{*}Ag(t-t^*)^2}\,a^{10},\tag{5.13}$$

$$\widehat{a^{20}}=\frac{1}{\alpha^{*2}A^2g^2(t-t^*)^4}\,a^{20}.\tag{5.14}$$

The coefficients are determined through a process illustrated as follows in spatio-temporal coordinates for simplicity. If one wants to construct a model in the form

https://doi.org/10.1017/jfm.2024.323 Published online by Cambridge University Press

(5.9), then four equations must be formulated to determine the four coefficients. This is done by using measurements from the four simulations used to determine the four moments D^{00}, D^{10}, D^{01} and D^{20}. For example, the first equation results from substitution of F^{00} for $-\langle v'Y'_H\rangle$ and the associated desired $\partial\langle Y_H\rangle/\partial y$; the remaining three equations follow, using the other three moments:

$$\left[1 + a^{10}\frac{\partial}{\partial y} + a^{01}\frac{\partial}{\partial t} + a^{20}\frac{\partial^2}{\partial y^2}\right]F^{00} = a^{00}, \tag{5.15}$$

$$\left[1 + a^{10}\frac{\partial}{\partial y} + a^{01}\frac{\partial}{\partial t} + a^{20}\frac{\partial^2}{\partial y^2}\right]F^{10} = a^{00}\left(y - \frac{1}{2}\right), \tag{5.16}$$

$$\left[1 + a^{10}\frac{\partial}{\partial y} + a^{01}\frac{\partial}{\partial t} + a^{20}\frac{\partial^2}{\partial y^2}\right]F^{01} = a^{00}t, \tag{5.17}$$

$$\left[1 + a^{10}\frac{\partial}{\partial y} + a^{01}\frac{\partial}{\partial t} + a^{20}\frac{\partial^2}{\partial y^2}\right]F^{20} = a^{00}\frac{1}{2}\left(y - \frac{1}{2}\right)^2. \tag{5.18}$$

This system of equations is then rearranged into a matrix equation $M_{MMI}\boldsymbol{a} = \boldsymbol{b}$, which is solved for the coefficients in vector $\boldsymbol{a} = (a^{00}, a^{10}, a^{01}, a^{20})^{\mathrm{T}}$. Note that this matrix equation is constructed over every point in space and time, so $\boldsymbol{a} = \boldsymbol{a}(y, t)$. In this work, analysis is done in self-similar coordinates, in which $\boldsymbol{a} = \boldsymbol{a}(\eta)$. If one wishes to construct a model with different moments, then the MMI operator and equations must be modified accordingly. For example, a model using only D^{00} and D^{10} would have an MMI operator of the form $1 + a_{10}(\partial/\partial y)$ and use only the first two equations (with the a^{01} and a^{20} terms removed). Thus models using different combinations of moments would use different MMI coefficients a^{mn}.

To summarize, for this implicit operator form, the following system of equations is solved in self-similar coordinates:

$$\mathcal{L}_{MMI}\left\{-\widehat{\langle v'Y'_H\rangle}\right\} = \widehat{a^{00}}\,\frac{\mathrm{d}\langle Y_H\rangle}{\mathrm{d}\eta}, \tag{5.19}$$

$$\frac{\mathrm{d}}{\mathrm{d}\eta}\left(-\widehat{\langle v'Y'_H\rangle}\right) = -2\eta\,\frac{\mathrm{d}\langle Y_H\rangle}{\mathrm{d}\eta}, \tag{5.20}$$

where $\mathcal{L}_{MMI}$ is the MMI operator constructed using some combination of moments, such as in (5.10). Numerically, the following system is solved:

$$P\left(-\widehat{\langle v'Y'_H\rangle}\right) = \widehat{a^{00}}\,\mathcal{D}_\eta\langle Y_H\rangle, \tag{5.21}$$

$$\mathcal{D}_\eta\left(-\widehat{\langle v'Y'_H\rangle}\right) = -2\eta\mathcal{D}_\eta\langle Y_H\rangle, \tag{5.22}$$

where P is the matrix representing the numerical MMI operator, and $\mathcal{D}_\eta$ is the matrix representing the numerical derivative with respect to η. This can be rewritten as a block matrix–vector multiplication:

$$M\boldsymbol{x} = \begin{bmatrix} P & -\widehat{a^{00}}\,\mathcal{D}_\eta \\ \mathcal{D}_\eta & 2\eta\mathcal{D}_\eta \end{bmatrix}\begin{bmatrix} -\widehat{\langle v'Y'_H\rangle} \\ \langle Y_H\rangle \end{bmatrix} = \boldsymbol{b}, \tag{5.23}$$

where $\boldsymbol{b}$ is a vector representing the right-hand side of (5.22), with the proper boundary conditions enforced. In this study, zero gradient boundary conditions are used for

https://doi.org/10.1017/jfm.2024.323 Published online by Cambridge University Press

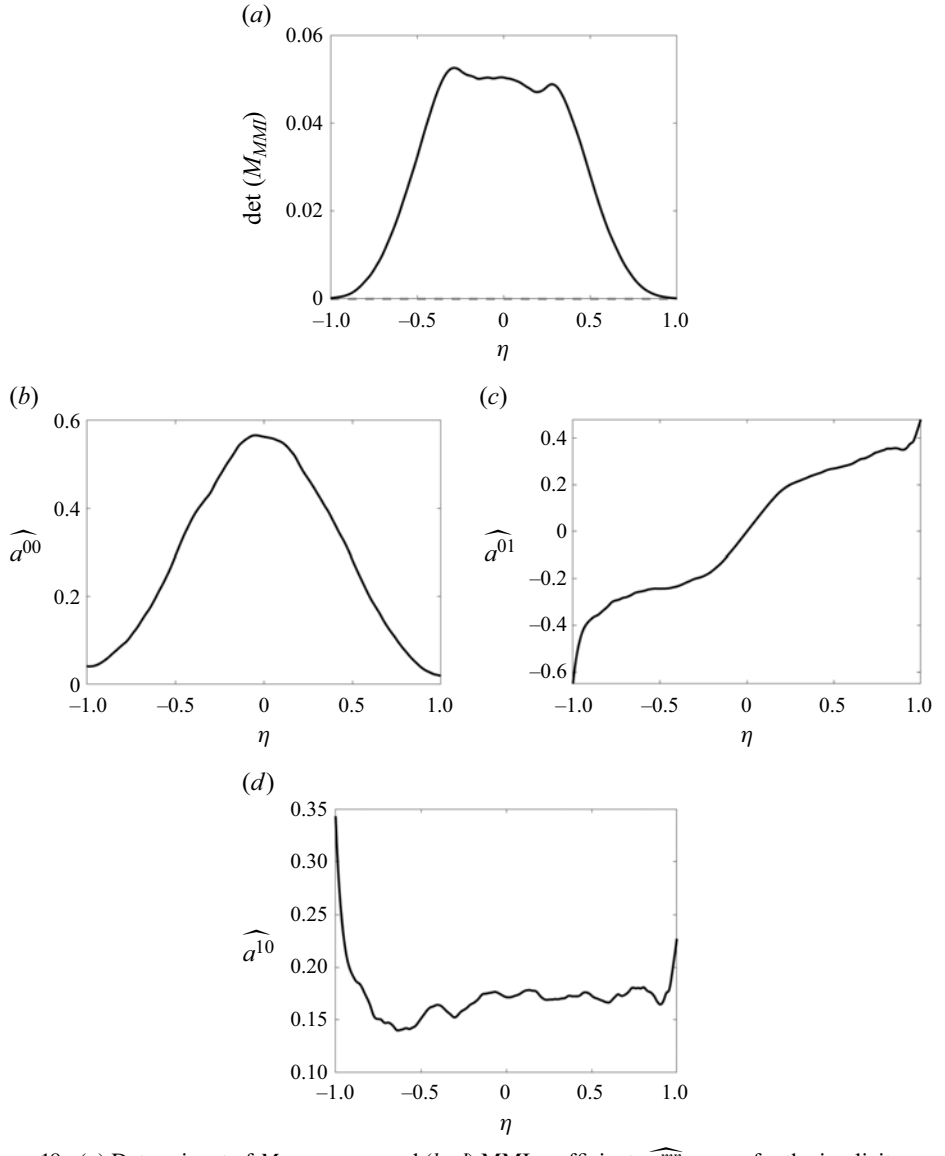

Figure 18. (*a*) Determinant of M_{MMI} over η and (*b–d*) MMI coefficients $\widehat{a^{mn}}$ over η for the implicit operator form using D^{00}, D^{10} and D^{01}.

the turbulent scalar flux, and Dirichlet boundary conditions are used for the mean concentration. The system is solved using finite differences on a staggered mesh.

Presented in this work are the determinants of the MMI matrix and resulting a_{mn} for two different combinations of moments. Figure 18 shows that with the combination of D^{00}, D^{10} and D^{01}, the determinant of the MMI matrix is positive for all η, so the a_{mn} are all well-behaved. This is indicative of good model form. On the other hand, figure 19 shows that with the combination of D^{00} and D^{01}, the determinant of the MMI matrix crosses zero, so the a_{mn} contain singularities that effect poor RANS predictions (observable in plots presented later). Singular matrices arising in the MMI solve for a certain form of the implicit operator form may indicate that form is poor, in the sense that the combination of moments does not make a good RANS model. Since MMI appears to be sensitive to

https://doi.org/10.1017/jfm.2024.323 Published online by Cambridge University Press

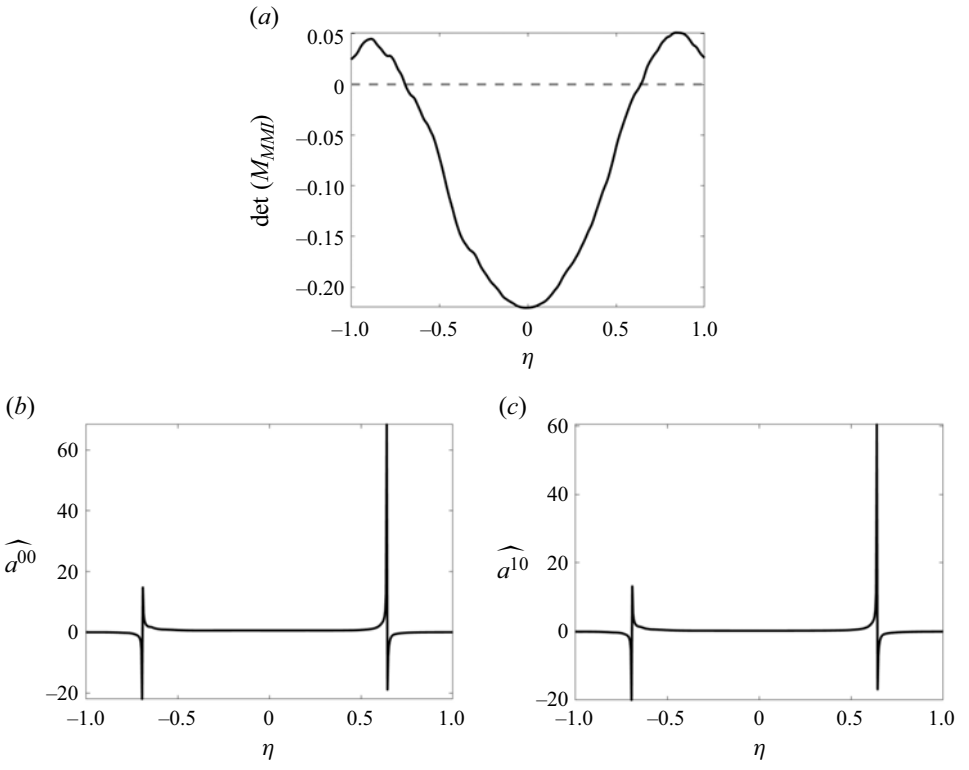

Figure 19. (*a*) Determinant of M_{MMI} over η and (*b*,*c*) MMI coefficients $\widehat{a^{mn}}$ over η for the implicit operator form using D^{00} and D^{01}. Here, M_{MMI} is singular at the η at which its determinant crosses zero.

the information that it takes in to determine the implicit operator coefficients, one must take special care and choose a model form that avoids this issue. It is found that MMI determinant zero crossings do not occur for any of the moment combinations tested in this work other than the D^{00} and D^{01} combination, but it may happen with combinations of other higher-order moments not measured here.

Turbulent scalar fluxes computed using the implicit operator form are shown in figure 20. The implicit operator form's turbulent scalar flux prediction using just D^{00} is identical to that of the explicit operator form, by construction. It is apparent that adding either D^{10} or D^{01} alone is insufficient. As noted earlier, adding D^{01} leads to a particularly poor prediction due to singular MMI matrices at some η. The best match to DNS is attained using the combination D^{00}, D^{10} and D^{01}. In fact, it is evident that the implicit operator form using D^{00}, D^{10} and D^{01} predicts the turbulent scalar flux more accurately than the explicit operator form using the same moments. This is because the implicit operator form is designed to match the shape of the eddy diffusivity kernel, and the explicit operator form may not be accomplishing this.

These trends in the explicit and implicit operator forms can be observed again in the predictions of the mean concentration profile, shown in figure 21. In particular, the implicit operator form using D^{00}, D^{10} and D^{01} gives a very good prediction of the mean concentration that nearly overlaps the DNS measurement. For a clearer comparison of the explicit and implicit operator forms using these moments, figure 22 shows the derivatives of the DNS- and model-computed $\langle Y_H \rangle$. The implicit operator form predicts a magnitude and shape closer to the DNS measurement than the explicit operator form does.

https://doi.org/10.1017/jfm.2024.323 Published online by Cambridge University Press

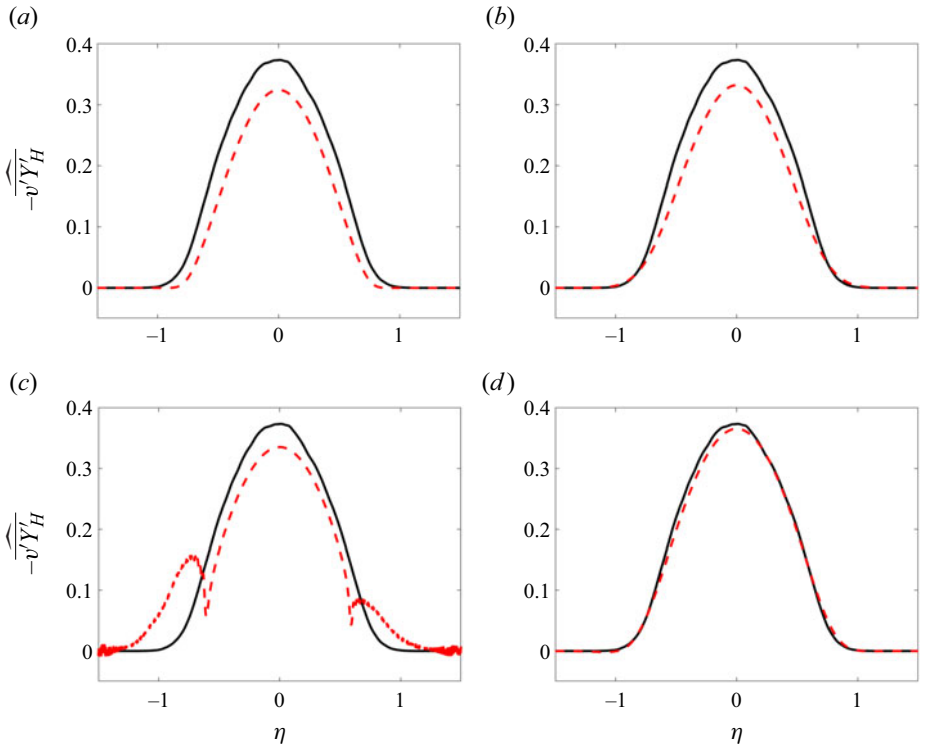

Figure 20. Turbulent scalar flux predictions using the implicit operator form. Moments of eddy diffusivity used in the model are: (*a*) D^{00}; (*b*) D^{00}, D^{10}; (*c*) D^{00}, D^{01}; (*d*) D^{00}, D^{10}, D^{01}.

In particular, the implicit operator form captures the shape of the tails much better than the explicit operator form.

6. Conclusion

In this assessment, it is determined that non-locality must be considered in developing more predictive models for RTI. The studies presented in this work are facilitated using MFM, a numerical tool for precisely measuring closure operators. Four of the eddy diffusivity moments of RTI (D^{00}, D^{10}, D^{01} and D^{20}) are measured, and it is demonstrated that the higher-order moments, which contain information about the non-locality of the eddy diffusivity kernel, should not be neglected when constructing models for RTI.

Specifically, it is determined that D^{00}, D^{10} and D^{01} are the most important moments for constructing a model for RTI. Two methods for constructing RANS models using these moments are presented. First, an explicit operator form, based on a Kramers–Moyal-like expansion derived by taking the Taylor series expansion of the scalar gradient in the generalized eddy diffusivity, is described and tested. While incorporation of higher-order moments in the explicit operator form results in more accurate predictions than a leading-order model, there exist several issues. One problem is that the expansion used for the explicit operator form may not converge, so addition of higher-order moments leads to less accurate predictions. Another problem is that the explicit operator form is difficult to implement numerically.

Thus an implicit operator form is presented to address these issues with the explicit operator form. Since an implicit operator form involves an invertible matrix operator, it

https://doi.org/10.1017/jfm.2024.323 Published online by Cambridge University Press

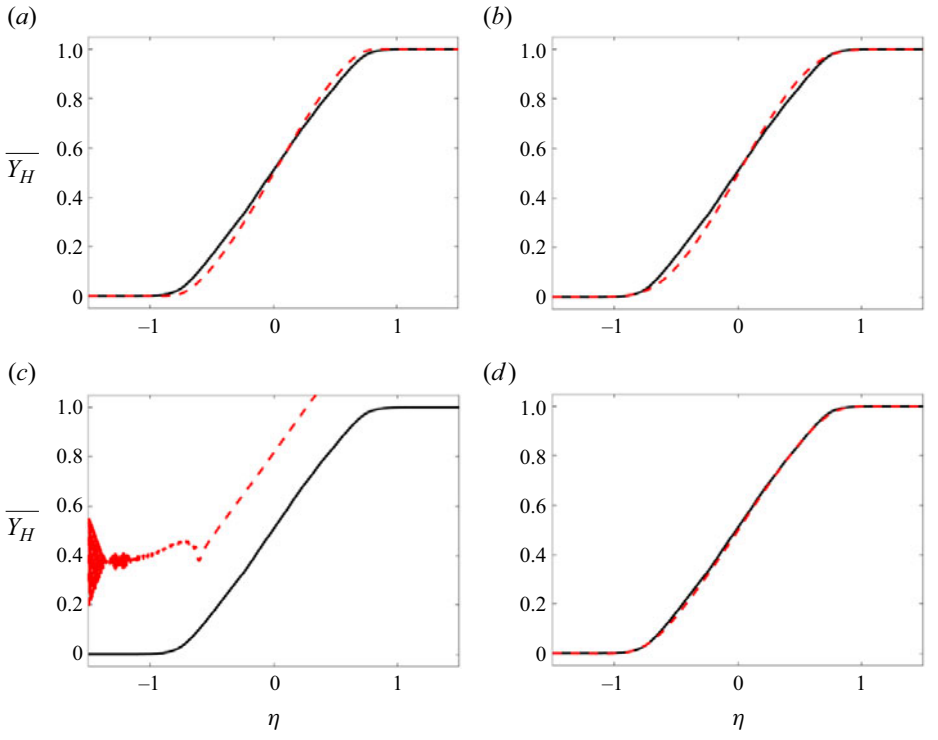

Figure 21. Mean concentration profile predictions using the implicit operator form. Moments of eddy diffusivity used in the model are: (*a*) D^{00}; (*b*) D^{00}, D^{10}; (*c*) D^{00}, D^{01}; (*d*) D^{00}, D^{10}, D^{01}.

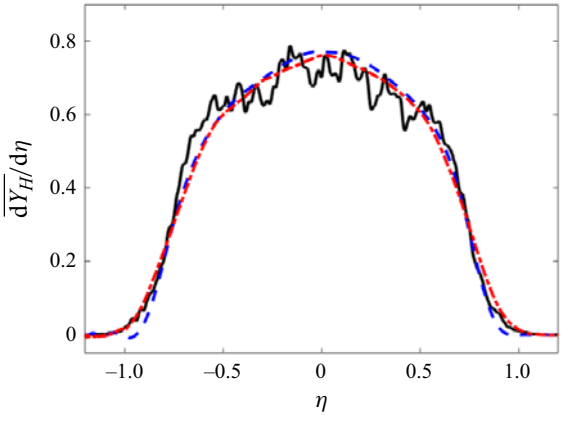

Figure 22. Derivatives of $\langle Y_H \rangle$ computed using DNS (solid black), an explicit operator form (dashed blue), and an implicit operator form (dash-dotted red).

is easier to implement than an explicit operator form. In addition, the proposed implicit operator form is designed to match the shape of the eddy diffusivity kernel via the MMI operator, in contrast to the explicit operator form, which truncates a non-converging Kramers–Moyal expansion. It is shown that the implicit operator form exhibits a marked improvement in predictions over the explicit operator form.

Incorporation of non-locality into RANS models via these operator forms comes with several challenges. For one, development of any new model must consider scalar realizability. While this is not thoroughly explored in this work, since an actual model

https://doi.org/10.1017/jfm.2024.323 Published online by Cambridge University Press

is not yet proposed, one approach to preserve realizability is suggested by Braun & Gore (2021), where the turbulent scalar flux is rewritten as an advection-like term and added to the original advection term in order to enforce physical mean component mass fractions; a conservative numerical scheme maintains realizability. Further, the new model must be tested on more complex RTI for it to be useful in practical settings such as ICF. This includes assessment of the model for 3-D, finite Atwood and compressible (Richtmyer–Meshkov) flows. The model should be tested in the same validation cases as other models for RTI, such as the tilted rig (Denissen *et al.* 2014) and gravity reversal (Banerjee, Gore & Andrews 2010). Based on these evaluations, which may also involve new MFM measurements where the method is extended to more complex flow regimes, the new model can be amended, as is the usual process of turbulence model development. This is left for future work, when a new model is developed based on the findings presented here.

One obstacle encountered in these studies is the inherent statistical error in the DNS computations. In particular, the higher-order moments contain high statistical error due to buildup of error from the lower-order moments on which they depend. Because of this, it is admittedly difficult to draw definite conclusions about the effect of higher-order moments beyond the first-order moments. That is, due to the statistical error, it is currently unclear if inclusion of moments beyond first order in a RANS model would significantly improve its predictions, or if just the first-order temporal and spatial moments along with the leading-order moment are sufficient. This motivates development of a technique to accelerate the statistical convergence of these higher-order moments. Such a method could also be used to study the effect of other higher-order moments that were not measured in this present work, since they would have suffered from high statistical error with the current method.

It must be stressed that the results in this work are for 2-D RTI and should not be applied directly to three dimensions. As noted previously, the third spatial dimension significantly impacts the turbulent physics of RTI. In particular, 3-D RTI has a lower growth rate than 2-D RTI, so lower magnitudes of the eddy diffusivity moments are expected in three dimensions. Despite the quantitative difference in physics between two and three dimensions, they are qualitatively similar in the RANS space, so trends in the shapes of the eddy diffusivity moments are expected to persist in three dimensions. In other words, the form of the turbulent scalar flux closure in three dimensions is expected to be the same as in two dimensions, but the coefficients would be different. These expected trends are yet to be confirmed, and future work should involve applying MFM to 3-D RTI.

Through this work, an understanding of non-locality in 2-D RTI has been developed. It has been shown that incorporation of information about the non-locality of the eddy diffusivity may greatly improve the accuracy of a RANS model. This work demonstrates this by testing operators using MFM measurements of the non-local eddy diffusivity. In practice, a RANS model for RTI would not have to rely on these MFM measurements directly; one would not have to perform many MFM simulations to construct a model. In other words, MFM should be seen as a diagnostic tool rather than the means for building the actual model. The ultimate goal is to develop an improved, more predictive model for RTI by incorporating non-local information, which the present work has demonstrated to be significant for accurate prediction of mean scalar transport in 2-D RTI.

Funding. This work was performed under the auspices of the US Department of Energy by Lawrence Livermore National Laboratory under contract no. DE-AC52-07NA27344. D.L. was additionally supported by

https://doi.org/10.1017/jfm.2024.323 Published online by Cambridge University Press

the Charles H. Kruger Stanford Graduate Fellowship. J.L. was additionally supported by the Burt and Deedee McMurtry Stanford Graduate Fellowship.

Declaration of interests. The authors report no conflict of interest.

Author ORCIDs.
D.L.O.-L. Lavacot https://orcid.org/0000-0002-3446-6015;
J. Liu https://orcid.org/0009-0006-3798-2839;
B.E. Morgan https://orcid.org/0000-0003-0170-1856;
A. Mani https://orcid.org/0000-0001-7497-9328.

Appendix A. Non-dimensionalizations

To determine the non-dimensionalizations in (3.24)–(3.28), a self-similarity analysis is performed. The following self-similarity coordinate is used:

$$\eta = \frac{y}{h_{fit}(t)} = \frac{y}{\alpha^* A g (t - t^*)^2}. \tag{A1}$$

To perform transformations to this self-similar space, all derivatives are written in terms of η:

$$\frac{\partial}{\partial t} = -\frac{2\eta}{t - t^*}\frac{\mathrm{d}}{\mathrm{d}\eta}, \tag{A2}$$

$$\frac{\partial}{\partial y} = \frac{1}{\alpha^* A g (t - t^*)^2}\frac{\mathrm{d}}{\mathrm{d}\eta}, \tag{A3}$$

$$\frac{\partial^2}{\partial t\,\partial y} = -\frac{2}{\alpha^* A g (t - t^*)^3}\left(\frac{\partial}{\mathrm{d}\eta} + \eta\frac{\mathrm{d}^2}{\mathrm{d}\eta^2}\right). \tag{A4}$$

To non-dimensionalize the eddy diffusivity moments, (3.6) is substituted into (3.3):

$$\frac{\partial\langle Y_H\rangle}{\partial t} = \frac{\partial}{\partial y}\left(D^{00}\frac{\partial\langle Y_H\rangle}{\partial y} + D^{10}\frac{\partial^2\langle Y_H\rangle}{\partial y^2} + D^{01}\frac{\partial^2\langle Y_H\rangle}{\partial t\partial y} + D^{20}\frac{\partial^3\langle Y_H\rangle}{\partial y^3} + \cdots\right). \tag{A5}$$

The equation is then transformed to self-similar space:

$$\begin{aligned}-\frac{2\eta}{t - t^*}\frac{\mathrm{d}\langle Y_H\rangle}{\mathrm{d}\eta} = \frac{1}{\alpha^* A g (t - t^*)^2}\frac{\mathrm{d}}{\mathrm{d}\eta}\Bigg[&\frac{1}{\alpha^* A g (t - t^*)^2}D^{00}\frac{\mathrm{d}\langle Y_H\rangle}{\mathrm{d}\eta} \\ &+ \frac{1}{\alpha^{*2}A^2g^2(t - t^*)^4}D^{10}\frac{\mathrm{d}^2\langle Y_H\rangle}{\mathrm{d}\eta^2} \\ &- \frac{2}{\alpha^* A g (t - t^*)^3}D^{01}\left(\frac{\mathrm{d}\langle Y_H\rangle}{\mathrm{d}\eta} + \eta\frac{\mathrm{d}^2\langle Y_H\rangle}{\mathrm{d}\eta^2}\right) \\ &+ \frac{1}{\alpha^{*3}A^3g^3(t - t^*)^6}D^{20}\frac{\mathrm{d}^3\langle Y_H\rangle}{\mathrm{d}\eta^3} + \cdots\Bigg].\end{aligned} \tag{A6}$$

https://doi.org/10.1017/jfm.2024.323 Published online by Cambridge University Press

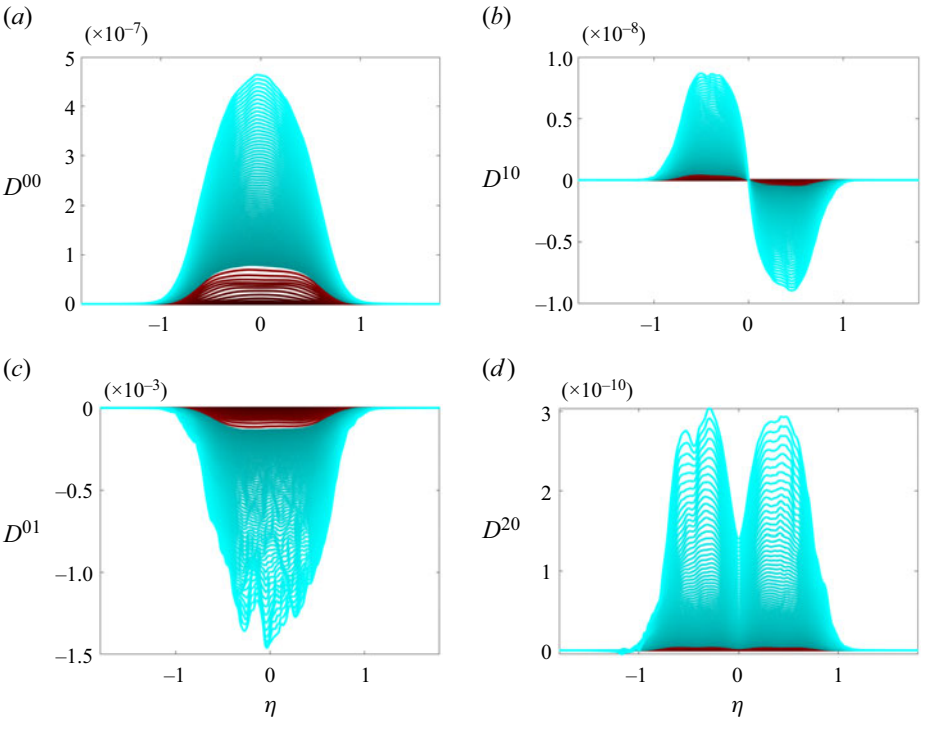

Figure 23. Unscaled moments at different times over x. Dimensions of the moments are as follows: D^{00} is $\mathrm{m}^2\,\mathrm{s}^{-1}$; D^{10} is $\mathrm{m}^3\,\mathrm{s}^{-1}$; D^{01} is m^2; and D^{20} is $\mathrm{m}^4\,\mathrm{s}^{-1}$. Red profiles are from early times, and cyan profiles are from late times, when the flow is self-similar. Lighter lines correspond to later times; darker lines correspond to earlier times.

Rearranging,

$$-2\eta\frac{\mathrm{d}\langle Y_H\rangle}{\mathrm{d}\eta} = \frac{\mathrm{d}}{\mathrm{d}\eta}\left[\frac{1}{\alpha^{*2}A^2g^2(t-t^*)^3}D^{00}\frac{\mathrm{d}\langle Y_H\rangle}{\mathrm{d}\eta} + \frac{1}{\alpha^{*3}A^3g^3(t-t^*)^5}D^{10}\frac{\mathrm{d}^2\langle Y_H\rangle}{\mathrm{d}\eta^2} - \frac{2}{\alpha^{*2}A^2g^2(t-t^*)^4}D^{01}\left(\frac{\mathrm{d}\langle Y_H\rangle}{\mathrm{d}\eta}+\eta\frac{\mathrm{d}^2\langle Y_H\rangle}{\mathrm{d}\eta^2}\right) + \frac{1}{\alpha^{*4}A^4g^4(t-t^*)^7}D^{20}\frac{\mathrm{d}^3\langle Y_H\rangle}{\mathrm{d}\eta^3}+\cdots\right]. \tag{A7}$$

This reveals non-dimensionalizations for the eddy diffusivity moments. The prefactors to the derivatives of $\langle Y_H\rangle$ on the right-hand side are denoted as the normalized eddy diffusivity moments $\widehat{D^{mn}}$.

The turbulent scalar flux scales with the leading-order term in (3.6). Substitution of the non-dimensionalization for D^{00} (3.25) into the leading-order term in (3.6) and transformation to self-similar coordinates gives the scaling for the turbulent scalar flux:

$$-\langle v'Y_H'\rangle \sim \alpha^* Ag(t-t^*)\,\widehat{D^{00}}\,\frac{\mathrm{d}\langle Y_H\rangle}{\mathrm{d}\eta}. \tag{A8}$$

https://doi.org/10.1017/jfm.2024.323 Published online by Cambridge University Press

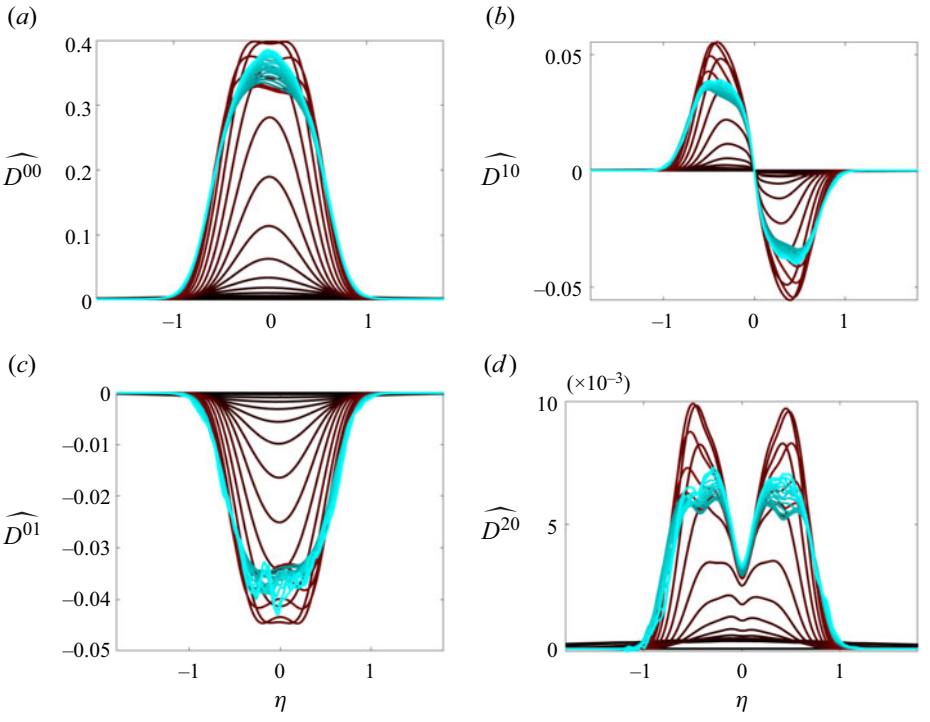

Figure 24. Self-similar collapse of moments. All $\widehat{D^{mn}}$ are dimensionless. Red profiles are from early times, and cyan profiles are from late times, when the flow is self-similar. Lighter lines correspond to later times; darker lines correspond to earlier times.

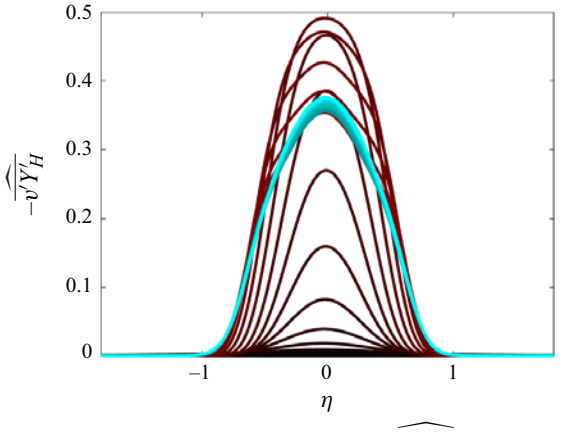

Figure 25. Self-similar collapse of turbulent scalar flux. Here, $-\widehat{\langle v'Y'_H\rangle}$ is dimensionless. Red profiles are from early times, and cyan profiles are from late times, when the flow is self-similar. Lighter lines correspond to later times; darker lines correspond to earlier times.

Figure 23 shows the unscaled moments measured directly from the MFM simulations. The profiles are taken from the portion of the simulation where the flow is self-similar ($\tau \gtrapprox 17$). It is obvious that without normalizing the moments as described above, there is no self-similar collapse. The moments are scaled and plotted against η in figure 24

https://doi.org/10.1017/jfm.2024.323 Published online by Cambridge University Press

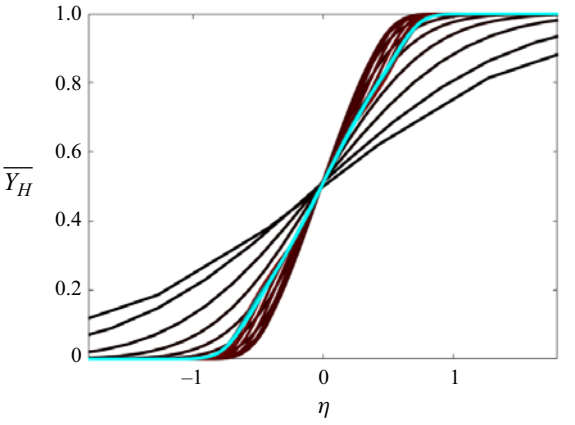

Figure 26. Mean concentration profiles at different times. Red profiles are from early times, and cyan profiles are from late times, when the flow is self-similar. Lighter lines correspond to later times; darker lines correspond to earlier times.

to demonstrate the self-similar collapse. The normalized turbulent scalar flux and mean concentration profiles are shown in figures 25 and 26, also showing self-similar collapse.

References

Banerjee, A., Gore, R.A. & Andrews, M.J. 2010 Development and validation of a turbulent-mix model for variable-density and compressible flows. *Phys. Rev.* E **82**, 046309.

Bender, J.D., *et al.* 2021 Simulation and flow physics of a shocked and reshocked high-energy-density mixing layer. *J. Fluid Mech.* **915**, A84.

Braun, N.O. & Gore, R.A. 2021 A multispecies turbulence model for the mixing and de-mixing of miscible fluids. *J. Turbul.* **22** (12), 784–813.

Cabot, W. 2006 Comparison of two- and three-dimensional simulations of miscible Rayleigh–Taylor instability. *Phys. Fluids* **18** (4), 045101.

Cabot, W.H. & Cook, A.W. 2006 Reynolds number effects on Rayleigh–Taylor instability with possible implications for type Ia supernovae. *Nat. Phys.* **2** (8), 562–568.

Casey, D.T., *et al.* 2014 Development of the CD SYMCAP platform to study gas–shell mix in implosions at the National Ignition Facility. *Phys. Plasmas* **21** (9), 092705.

Clark, T.T., Harlow, F.H. & Moses, R.W. 1997 Comparison of a spectral turbulence model with experimental data of Rayleigh–Taylor mixing. *Tech. Rep.* Los Alamos National Lab. (LANL), Los Alamos, NM (USA).

Clark, T.T. & Spitz, P.B. 1995 Two-point correlation equations for variable density turbulence. *Tech. Rep.* Los Alamos National Lab. (LANL), Los Alamos, NM (USA).

Cook, A.W., Cabot, W. & Miller, P.L. 2004 The mixing transition in Rayleigh–Taylor instability. *J. Fluid Mech.* **511**, 333–362.

Cook, A.W. & Dimotakis, P.E. 2001 Transition stages of Rayleigh–Taylor instability between miscible fluids. *J. Fluid Mech.* **443**, 69–99.

Cook, A.W. & Zhou, Y. 2002 Energy transfer in Rayleigh–Taylor instability. *Phys. Rev.* E **66** (2), 026312.

Darlington, R.M., McAbee, T.L. & Rodrigue, G. 2002 Large eddy simulation and ALE mesh motion in Rayleigh–Taylor instability simulation. *Comput. Phys. Commun.* **144** (3), 261–276.

Denissen, N.A., Rollin, B., Reisner, J.M. & Andrews, M.J. 2014 The tilted rocket rig: a Rayleigh–Taylor test case for RANS models. *Trans. ASME J. Fluids Engng* **136** (9), 091301.

Dimonte, G. & Tipton, R. 2006 *K-L* turbulence model for the self-similar growth of the Rayleigh–Taylor and Richtmyer–Meshkov instabilities. *Phys. Fluids* **18** (8), 085101.

Dimotakis, P.E. 2000 The mixing transition in turbulent flows. *J. Fluid Mech.* **409**, 69–98.

Gauthier, S. & Bonnet, M. 1990 A k-ε model for turbulent mixing in shock-tube flows induced by Rayleigh–Taylor instability. *Phys. Fluids* A **2** (9), 1685–1694.

Gull, S.F. 1975 The X-ray, optical and radio properties of young supernova remnants. *Mon. Not. R. Astron. Soc.* **171** (2), 263–278.

https://doi.org/10.1017/jfm.2024.323 Published online by Cambridge University Press

HAMBA, F. 1995 An analysis of nonlocal scalar transport in the convective boundary layer using the Green's function. *J. Atmos. Sci.* **52** (8), 1084–1095.

HAMBA, F. 2004 Nonlocal expression for scalar flux in turbulent shear flow. *Phys. Fluids* **16** (5), 1493–1508.

HAMBA, F. 2022 Analysis and modelling of non-local eddy diffusivity for turbulent scalar flux. *J. Fluid Mech.* **950**, A38.

KHAN, S.F., *et al.* 2016 Symmetry tuning of a near one-dimensional 2-shock platform for code validation at the National Ignition Facility. *Phys. Plasmas* **23** (4), 042708.

KRAICHNAN, R.H. 1987 Eddy viscosity and diffusivity: exact formulas and approximations. *Complex Syst.* **1** (4–6), 805–820.

KURIEN, S. & PAL, N. 2022 The local wavenumber model for computation of turbulent mixing. *Phil. Trans. R. Soc.* A **380** (2219), 20210076.

LAUNDER, B.E. & SPALDING, D.B. 1974 The numerical computation of turbulent flows. *Comput. Meth. Appl. Mech. Engng* **3** (2), 269–289.

LAVACOT, D.L.O.-L., LIU, J., MORGAN, B.E. & MANI, A. 2022 Continuing investigations of nonlocality in Rayleigh–Taylor instability using the macroscopic forcing method. In *75th APS DFD Conference, 20–22 November*, Bulletin of the American Physical Society, vol. 67, no. 19.

LINDL, J. 1995 Development of the indirect-drive approach to inertial confinement fusion and the target physics basis for ignition and gain. *Phys. Plasmas* **2** (11), 3933–4024.

LIU, J., WILLIAMS, H. & MANI, A. 2023 Systematic approach for modeling a nonlocal eddy diffusivity. *Phys. Rev. Fluids* **8** (12), 124501.

MANI, A. & PARK, D. 2021 Macroscopic forcing method: a tool for turbulence modeling and analysis of closures. *Phys. Rev. Fluids* **6**, 054607.

MAURI, R. 1991 Dispersion, convection, and reaction in porous media. *Phys. Fluids* A **3** (5), 743–756.

MORGAN, B.E. 2018 Response to 'Comment on "Large-eddy simulation and unsteady RANS simulations of a shock-accelerated heavy gas cylinder" by B.E. Morgan, J. Greenough'. *Shock Waves* **28** (6), 1301–1302.

MORGAN, B.E. 2022 Large-eddy simulation and Reynolds-averaged Navier–Stokes modeling of three Rayleigh–Taylor mixing configurations with gravity reversal. *Phys. Rev.* E **106**, 025101.

MORGAN, B.E. & BLACK, W.J. 2020 Parametric investigation of the transition to turbulence in Rayleigh–Taylor mixing. *Physica* D **402**, 132223.

MORGAN, B.E. & GREENOUGH, J.A. 2015 Large-eddy and unsteady RANS simulations of a shock-accelerated heavy gas cylinder. *Shock Waves* **26** (4), 355–383.

MORGAN, B.E., OLSON, B.J., BLACK, W.J. & MCFARLAND, J.A. 2018 Large-eddy simulation and Reynolds-averaged Navier–Stokes modeling of a reacting Rayleigh–Taylor mixing layer in a spherical geometry. *Phys. Rev.* E **98** (3), 033111.

MORGAN, B.E., OLSON, B.J., WHITE, J.E. & MCFARLAND, J.A. 2017 Self-similarity of a Rayleigh–Taylor mixing layer at low Atwood number with a multimode initial perturbation. *J. Turbul.* **18** (10), 973–999.

MUESCHKE, N.J., ANDREWS, M.J. & SCHILLING, O. 2006 Experimental characterization of initial conditions and spatio-temporal evolution of a small-Atwood-number Rayleigh–Taylor mixing layer. *J. Fluid Mech.* **567**, 27–63.

MUESCHKE, N.J. & SCHILLING, O. 2009 Investigation of Rayleigh–Taylor turbulence and mixing using direct numerical simulation with experimentally measured initial conditions. I. Comparison to experimental data. *Phys. Fluids* **21** (1), 014106.

OLSON, B.J. & GREENOUGH, J.A. 2014 Comparison of two- and three-dimensional simulations of miscible Richtmyer–Meshkov instability with multimode initial conditions. *Phys. Fluids* **26** (10), 101702.

PAL, N., KURIEN, S., CLARK, T.T., ASLANGIL, D. & LIVESCU, D. 2018 Two-point spectral model for variable-density homogeneous turbulence. *Phys. Rev. Fluids* **3**, 124608.

PARISH, E.J. & DURAISAMY, K. 2017 Non-Markovian closure models for large eddy simulations using the Mori–Zwanzig formalism. *Phys. Rev. Fluids* **2**, 014604.

PARK, D., LIU, J. & MANI, A. 2022 Direct measurement of the eddy viscosity tensor in a canonical separated flow: what is the upper bound of accuracy for local Reynolds stress models? In *AIAA SCITECH 2022 Forum*. AIAA.

PARK, D. & MANI, A. 2023*a* Direct calculation of the eddy viscosity operator in turbulent channel flow at $Re_\tau = 180$. *J. Fluid Mech.* (in review). arXiv:2108.10898.

PARK, D. & MANI, A. 2023*b* Direct measurement of the eddy viscosity tensor in a turbulent separation bubble with sweep. In *AIAA AVIATION 2023 Forum*, p. 3268. AIAA.

PAWULA, R.F. 1967 Approximation of the linear Boltzmann equation by the Fokker–Planck equation. *Phys. Rev.* **162**, 186–188.

POPE, S.B. 2001 Turbulent flows. *Meas. Sci. Technol.* **12** (11), 2020–2021.

RISTORCELLI, J.R. & CLARK, T.T. 2004 Rayleigh–Taylor turbulence: self-similar analysis and direct numerical simulations. *J. Fluid Mech.* **507**, 213–253.

https://doi.org/10.1017/jfm.2024.323 Published online by Cambridge University Press

ROMANOF, N. 1985 Application of the orthonormal expansion. In *Proceedings of the seventh conference on probability theory: Aug. 29–Sept. 4, 1982, Braşov, Romania* (ed. M. Iosifescu, Ş. Grigorescu & T. Postelnicu), p. 493. VSP.

SAWFORD, B.L. 2004 Conditional scalar mixing statistics in homogeneous isotropic turbulence. *New J. Phys.* **6** (1), 55.

SHARP, R.W. JR. & Barton, R.T. 1981 Hemp advection model. *Tech. Rep.* Lawrence Livermore Laboratory.

SHENDE, O.B., STORAN, L. & MANI, A. 2023 A model for drift velocity mediated scalar eddy diffusivity in homogeneous turbulent flows. *J. Fluid Mech.* (accepted). arXiv:2310.16372.

SHIRIAN, Y. 2022 Application of macroscopic forcing method (MFM) for revealing turbulence closure model requirements. PhD thesis, Stanford University.

SHIRIAN, Y. & MANI, A. 2022 Eddy diffusivity operator in homogeneous isotropic turbulence. *Phys. Rev. Fluids* **7**, L052601.

STEINKAMP, M.J., CLARK, T.T. & HARLOW, F.H. 1999*b* Two-point description of two-fluid turbulent mixing – I. Model formulation. *Intl J. Multiphase Flow* **25** (4), 599–637.

STEINKAMP, M.J., CLARK, T.T. & HARLOW, F.H. 1999*a* Two-point description of two-fluid turbulent mixing – II. Numerical solutions and comparisons with experiments. *Intl J. Multiphase Flow* **25** (4), 639–682.

TAYLOR, G.I. 1922 Diffusion by continuous movements. *Proc. Lond. Math. Soc.* **2** (1), 196–212.

YOUNG, Y.-N., TUFO, H., DUBEY, A. & ROSNER, R. 2001 On the miscible Rayleigh–Taylor instability: two and three dimensions. *J. Fluid Mech.* **447**, 377–408.

YOUNGS, D.L. 1994 Numerical simulation of mixing by Rayleigh–Taylor and Richtmyer–Meshkov instabilities. *Laser Part. Beams* **12** (4), 725–750.

ZHOU, Y. 2017 Rayleigh–Taylor and Richtmyer–Meshkov instability induced flow, turbulence, and mixing. II. *Phys. Rep.* **723–725**, 1–160.

https://doi.org/10.1017/jfm.2024.323 Published online by Cambridge University Press